Study of the interlaminar fracture under mode I loading on 3D printed parts

João Vidal Fonseca

Masters Dissertation

Supervisor: Prof. Marcelo Moura

Advisor: Eng. Isaac Ferreira

U.PORTO
FEUP FACULDADE DE ENGENHARIA
UNIVERSIDADE DO PORTO

Integrated Masters in Mechanical Engineering

June of 2018

Resumo

Nesta dissertação é proposta uma metodologia para a análise da tenacidade à fratura sob solicitações de modo I para provetes fabricados por impressão 3D, especificamente para o processo FDM (Fused Deposition Modelling). Este trabalho surge pela necessidade iminente de melhoria deste processo, de modo a que este possa abranger a gama de aplicações na qual o requisito fundamental é um bom desempenho em termos mecânicos.

Com este intuito, foi dimensionada uma geometria específica tendo em conta as características do material e processo utilizados, para a realização de testes DCB (Double Cantilever Beam). Foram efetuadas três séries de testes experimentais, sendo que em paralelo foi também feita uma análise numérica aos dados obtidos. Posteriormente, foi feita uma análise por microscópio às superfícies de fratura resultantes dos testes experimentais, com vista ao refinamento das conclusões e a um melhor entendimento das variáveis das quais depende o processo. Os resultados obtidos indicam um valor consistente para a tenacidade à fratura apenas no caso do material não reforçado. No entanto foi possível obter um conjunto de razões que justificam o comportamento observado no caso do material reforçado. As ferramentas de análise numérica utilizadas revelaram-se também adequadas para o estudo desta combinação específica de material e processo.

Por fim, um conjunto de soluções foi apresentado tendo em vista o aperfeiçoamento do processo visado, dado que este se encontra numa fase relativamente inicial de desenvolvimento.

Study of the interlaminar fracture under mode I loading on 3d printed parts

Abstract

In this dissertation, a methodology for the analysis of the fracture toughness under mode I loading for 3D printed specimens is proposed, aimed specifically the fused deposition modelling process. This work is contextualized by the urgent need of improvement in this area, in order to extend the viability of this process to applications which require high mechanical performance.

For this purpose, a specific geometry was dimensioned, taking into account the inherent characteristics of both the material and process applied, for the realization of double cantilever beam tests. Three series of experimental tests were made, being that in parallel a numerical analysis was also followed for each series. Posteriorly, an inspection on the fracture surfaces resulting from the experimental tests was made, by microscopy, in order to refine the conclusions obtained and furtherly comprehend the variables in play. The obtained results provided a consistent value for the fracture toughness for only one of the cases studied, being this the unreinforced material. However, for the reinforced material, a set of conclusions which justify its behaviour was also able to be obtained. In addition to this, the method followed for the numerical analysis also revealed itself as suitable for this specific combination of material and process.

Lastly, a set of conclusions was presented, aimed for the improvement of the applied process, which is still in a relatively initial phase of development.

Acknowledgments

First of all, I would like to thank professor Marcelo Moura, for his dedication and for being at disposal to help at all times, for every problem encountered through the course of this dissertation. I would also like to express my gratitude for all the guidance and knowledge provided.

To engineer Isaac Ferreira, I would like to thank for all the support given throughout the dissertation, not only by the expertise in additive manufacturing, but also for helping me in every decision involved with the experimental work.

To engineers Filipe Silva and Raul Moreira, for all the assistance given in the numerical analysis as well as in every aspect related to the experimental tests. For the know-how and help supplied in both areas, and also for helping in my integration within INEGI.

To my family, especially my parents, I want to thank all the emotional support given throughout the years, and all the teachings which shaped me into the person I am today. For always being concerned with my well-being, as well as my success. For always making an effort to give me the best chance at succeeding, even in the hardest times.

To my friends, for all the advice and help given, for the course of the dissertation. For always being present in the good and bad times, and for making my experience in university an unforgettable one.

To my girlfriend, for all the patience, confidence and assistance given during the realization of this project. For being a source of serenity in every moment, and for the comprehension shown.

Lastly, I would like to express my gratitude for being granted the opportunity to be part of an ongoing research project, which I regard as a valuable experience for me.

Author gratefully acknowledge the funding of Project NORTE-01-0145-FEDER-000022 -Scitech – Science and Technology for Competitive and Sustainable Industries, cofinanced by Programa Operacional Regional do Norte (NORTE2020), through Fundo Europeu de Desenvolvimento Regional (FEDER).

Author gratefully acknowledge the funding of Project POCI-0145-FEDER-016414 - FIBR3D- Additive manufacturing based on hybrid processes for long or continuous fibre reinforced polymeric matrix composites, cofinanced by Programa Operacional Regional de Lisboa (LISBOA 2020), through Fundo Europeu de Desenvolvimento Regional (FEDER) and through National Funds from FCT – Fundação para a Ciência e Tecnologia.

Index

Nomenclature

3D	Three Dimensional
A	Cracked area
a	Observed crack length
a_0	Pre-crack length
a_e	Equivalent crack length
ABS	Acrylonitrile Butadiene Styrene
AM	Additive Manufacturing
ASTM	American Society for Testing and Materials
B	Width
C	Compliance
CAD	Computer Aided Design
CBBM	Compliance-Based Beam Method
CCM	Compliance Calibration Method
CNC	Computer Numerical Control
d	Damage parameter
D	Damage matrix
DCB	Double Cantilever Beam
DEGI	Department of Engineering and Industrial Management
DEMec	Department of Mechanical Engineering
E	Stiffness matrix
E_1	Young modulus
E_f	Corrected Young modulus
FDM	Fused Deposition Modelling
FEUP	Faculty of Engineering of the University of Porto
FFF	Fused Filament Fabrication
FPZ	Fracture Process Zone
G	Energy release rate
G_c	Critical energy release rate
G_I	Energy release rate for mode I
G_{LR}	Shear modulus
h	Height
I	Second moment of area
I	Identity matrix

L	Length
MBT	Modified Beam Theory
P	Test load
PA12	Polyamide 12
PC	Polycarbonate
PLA	Polylactic Acid
R	Resistance
sCF	Short Carbon Fibre
STL	Standard Triangulation Language
U	Strain energy
W	Work performed

δ	Test displacement
$\delta_{j,\mathrm{I}}$	Cohesive law relative displacement (j =1, 2, u) for pure mode I
$\sigma_{j,\mathrm{I}}$	Local cohesive strength (j =1, 2, u) for pure mode I

Figure index

Table index

1 Introduction

1.1 Introduction and motivation

Fused deposition modelling (FDM), one of the most popular additive manufacturing (AM) techniques, has been regarded as an effective method for the creation of complex geometries. However, as it can be understood from the production process, which relies on creating the desired geometry layer by layer, the interfacial bonding strength between the mentioned layers plays an important role on the mechanical properties of the resulting part. Since each layer is created by deposition of a line of extruded filament in a defined orientation, this process is also prone to induce manufacturing defects, such as voids or air gaps. In fact, one of the major issues when applying this technique is the highly anisotropic behaviour exhibited by the created parts, which is undesirable when the demanded application requires a high mechanical performance. This effect is considered to be one of the major limitations in the current state of art for this process, since it limits its applicability to aesthetic and low load components. As it can be perceived by this conclusion, it is important to develop solutions from which higher mechanical properties can be obtained, in order to increase its viability for this type of applications.

1.2 Presentation of the host institution

This dissertation was conducted at the Institute of Science and Innovation in Mechanical engineering and Industrial Engineering (INEGI), in association with the Department of Mechanical Engineering (DEMec) of the Faculty of Engineering of the University of Porto (FEUP). It was developed in the scope of a research project entitled FIBR3D - Additive manufacturing based on hybrid processes for long or continuous fibre reinforced polymeric matrix composites.

1.3 Objectives of this work

This work's main purpose is to study the bond connection between layers, i.e., the interlaminar strength and toughness under mode I loading at these critical interfaces, of components created by the FDM process. In order to do this, an analysis via fracture mechanics

concepts will be applied, for the characterization of the crack propagation behaviour presented by a series of experimental tests. This is done in order to search and adequate a method from which the correct measurement of the fracture toughness can be obtained. The aim is to present measures that can be taken to enhance it, since it is the main property responsible for the characterization of the fracture between layers.

1.4 Methodology carried

The method carried out for this dissertation can be regarded as a set of tasks:

- **Literature review:** Firstly, an analysis on state of the art concerning the subjects involved was conducted. This was done in order to point out the main weaknesses of the process and furtherly comprehend the results obtained, as well as to identify the areas requiring development.
- **Experimental process:** Afterwards, a geometry suitable for both the material and experimental test applied was firstly created, taking into account the conditions imposed by the manufacture process (FDM). This was followed by a series of experimental tests, which provided the data for analysis, being that the second and third series were employed as a way to verify the results obtained initially.
- **Numerical analysis:** In this stage, the obtained experimental data was analysed and compared to a set of values generated numerically, through the use of fracture characterization models. This was done in order to search and adequate a method for this type of technology and material.
- **Discussion and results:** In this step, a comparison between the experimental and numerical data was made, and the surfaces of the specimens were analysed through microscopy. This allowed the identification of the main flaws for the experimental process, and an overall appreciation of the set of data obtained, taking into account other research made in this area.
- **Conclusion and future works:** Lastly, a set of conclusions about the behaviour of this type of material for the applied manufacture process was obtained, followed by the presentation of possible steps to be made for the enhancement of this technology.

1.5 Structure of the dissertation

This dissertation consists of six chapters, which are summarized by the following structure and by the appendix A, which contains a Gantt chart:

- **Chapter 1 (Introduction) –** In this chapter the dissertation is presented and contextualized to the reader, by a brief description of the followed methodology and reasons which fundament its importance for the current moment.
- **Chapter 2 (Literature review) –** In this section, the state of the art of the subjects involved in this dissertation is presented, being these the FDM production process, aimed specifically for the materials involved, (polyamide 12 and its carbon fibre reinforced version), and the fracture mechanics concepts applied to the post analysis.
- **Chapter 3 (Experimental work) –** The performed experimental work is developed and explained, being the main objective the successful evaluation of the fracture toughness of the specimens created by the 3D printer.
- **Chapter 4 (Numerical analysis) –** The concepts used for the numerical analysis are explained in detail, in order to allow a better comprehension of the work done.
- **Chapter 5 (Results and discussion) -** In this chapter, a comparison between the experimental and numerical data is carried out. This is done in order to search and adequate a methodology for the characterization of this specific combination of material and technology, as well as to point out the main problems found through the course of the dissertation, and furtherly discuss them based on what has been done in this area.
- **Chapter 6 (Concluding remarks) –** Lastly, a summarized description of the work done is presented, followed by the main conclusions obtained and suggestions for future works.

2 Literature review

2.1 Fused deposition modelling (FDM)

This type of technology is the resulting evolutionary process of the rapid prototyping concept, which was introduced in the mid 1980's, and was originally applied for the creation of prototypes in the early stages of development. However, due to evolutions in the materials and processes associated to it, in conjunction with cost reductions of the technologies applied, this concept rapidly branched out into several categories, each with its particularities. In result of this, a new type of manufacturing concept was created, being this the additive-manufacturing (AM). For this dissertation, the Fused Deposition Modelling (FDM) process was applied, which is, in the current moment, the most used technique of the AM concept, due to being relatively simple when comparing to the other available options. This additive-manufacturing technology, which is also known as fused filament fabrication (FFF), was created in 1989 by the founder of the Stratasys company. It creates parts layer by layer, from the bottom to the top, by the extrusion of heated thermoplastic filaments.

This process begins by the creation of a 3D model of the desired component, by computer aided design (CAD). This type of software allows the exportation of the resulting model to the STL (stereolithography) format, which contains its geometry information. Afterwards, it is processed by specific 3D printing software, such as Cura or simplify3D, which slices the model into horizontal layers, as exemplified by Figure 1.

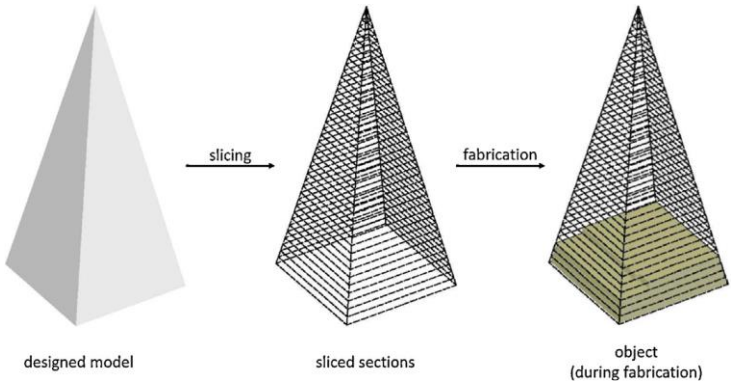

Figure 1 – Schematic of the additive manufacturing concept. [1]

2.1.1 FDM processing parameters

This type of software also allows the user to define a series of parameters which are directly associated with the quality of the final printed component. These parameters can be divided in two main categories: the FDM parameters, in which the process is adjusted to the specific material used, and the printing parameters, where all the variables related to the geometry of the material can be defined.

For the first category, it is important to mention that this process is limited to the use of thermoplastic polymers within a defined melt viscosity range. This is due to the technological process applied, which requires the molten viscosity to be high enough to allow the printing of accurately dimensional components, and low enough to allow the filament to be extruded [2]. As it can be concluded by these conditions, this limits the applicability of the FDM technology, being the most commonly used polymers the ABS, PLA, and PC. In this dissertation, however, the polymer chosen was the polyamide 12 in its pure form, and its reinforced version with short carbon fibres. In Figure 2, a schematic design of the typical build for this type of machine is presented.

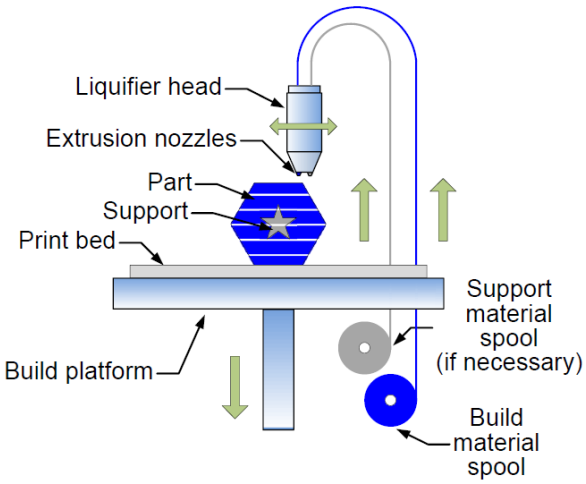

Figure 2 – Schematic representation of the FDM process. [3]

As evidenced by the figure, the material used is initially in a solid state, coiled in a spool, in the form of a filament. Before the print starts, the liquefier head and the print bed are heated to a pre-defined temperature, specific to the material applied. The first is done in order for the material to be able to be extruded in a semi-liquid state; the second to promote the adhesion of the first printed layer to the extruded bed, to reduce the warping effect created by the thermal gradient induced by the different layer temperatures, as the printing process goes on. When the pre-heating stage is completed, the filament is pulled into the liquefier head, rapidly melting, and, as more solid material enters the liquefier, the molten one is forced to advance. This forces the material onto the extrusion nozzle, which is then distributed according to the second category of parameters mentioned in the beginning of this section. In Table 1, the printing parameters responsible for the geometry of the resulting FDM printed specimens are presented, along with its definition.

Table 1 – FDM printing parameters [4], [5].

Parameter	Definition
Part building orientation	Refers to the position of the specimen to be built, in order to X, Y, and Z-axis. Z is considered the direction of growth, perpendicular to the building platform, while X and Y are parallel to it.
Raster angle	The direction of the raster pattern applied, relative to X-axis of the building platform. In this dissertation, +45º/-45º in alternate layers will be applied, which is a common solution.
Raster/bead width	The width of the raster pattern applied to fill each layer's interior.
Raster to raster air gap	The gap between two adjacent rasters of the same layer. For a 100% infill rate, the supposed gap value is zero, being that this value cannot be exactly specified, due to the inherent characteristics of the applied materials.
Slice/Layer thickness	The thickness of a single layer deposited by the nozzle, being dependent from it.
Number of perimeters	Each layer's building process starts from the deposition of filament along the edges of the specimen, with each perimeter being deposited in the inner edge of the previously deposited one, taking the gap value into consideration.

The presented concepts are illustrated in Figure 3, in order to allow a further understanding of what was explained.

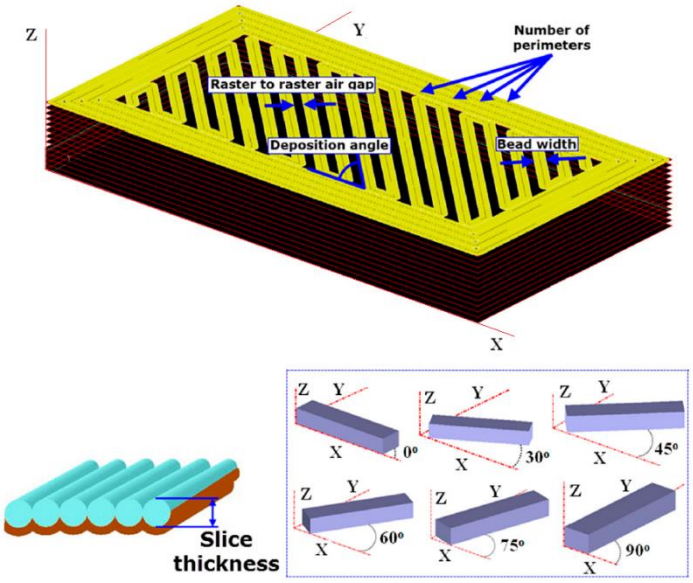

Figure 3 – Illustration of the FDM printing parameters [4].

With the definition of these parameters, the printing software is able to create a G-code file, which is essentially a set of computer numerical control (CNC) language instructions, considering the geometry and the variables presented earlier. This resulting file is then transferred onto the FDM machine software, and the 3D component designed initially is created, with the build platform descending the pre-defined height each time a layer is created.

2.1.2 FDM components structure

Due to the experimental tests and post-analysis which will be made on the resulting printed components, it is required to consider the current state of the art for this process. In fact, this technology is dependent on many variables, which can lead to poor performing components if not addressed correctly. For instance, it can be perceived from what was presented in section 2.1 that the thermal gradient induced by the continuous deposing of filament can play a huge role in the outcome of the component, dimensionally wise [6]. This effect also characterizes the interlayer adhesion strength of the component, since it dictates the type of bond created between adjacent layers while the deposition is occurring. Taking these factors into account, a schematic of the processes involved during the deposition is presented, in Figure 4.

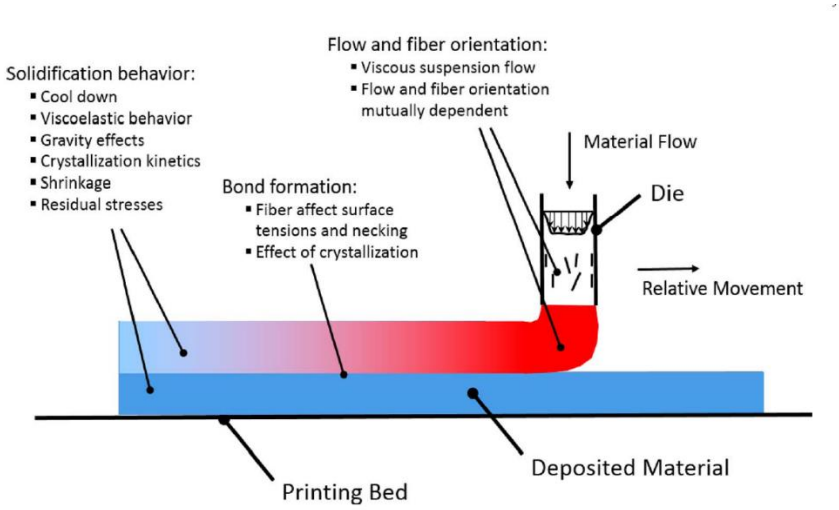

Figure 4 – Physical phenomena of the FDM process. [7]

As evidenced, the process of interlayer bonding in FDM process is rather complex. In result of the research in this area, there are a few guidelines for the printing process that must be acknowledged, in order to achieve a good interlayer adhesion. The experimental work, which will be made in a commercially available 3D printer, can be regarded as the classic FDM process, without access to additional energy sources. Thus, the newly deposited material is responsible for its bond, since it provides the energy source for it to happen [7]. In Figure 5, the main stages of the bond can be observed.

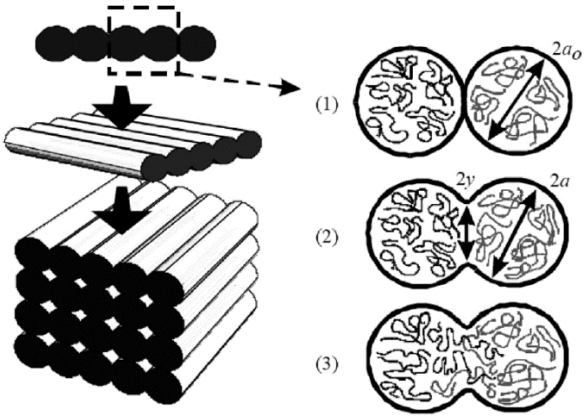

Figure 5 – Bond formation between filaments: (1) surface contact, (2) neck growth stage, (3) diffusion on the interface. [8]

As perceived by the illustration of the process, the bond between layers can be increased if a lower deposition rate is employed, since when doing so, the energy provided to the overall bonding strength is also increased. This conclusion, while bringing the advantage of creating a greater interlayer bonding adhesion, can also be costly, since by lowering the deposition rate, a greater thermal gradient is induced in the overall component, which can negatively influence the resulting component mechanical properties [9]. Also, as perceived by Figure 5, the bonding between layers inevitably contains a residual percentage of void space, which can create undesirable stress intensity points, thus, reducing the overall interlayer adhesion of the final component [10]. In conclusion, this connection can be regarded as a set of linking points, being these the bonds described before.

With the inclusion of fibres, the characterization of the bond formation becomes even more complex, due to the input of a new variable in the process. Since this is the case for this dissertation, this issue is required to be addressed, in order to prevent possible problems while printing, and to be able to fully understand the set of data that will be obtained. There are, in fact, issues derived from the use of reinforced filaments. Regarding the filament flow during the component print, the fibre can be viewed as the inclusion of an incompressible rigid body and are mainly deposed in the flow direction [11], as it is evidenced by the Figure 6, which aims to characterize this process through a simulation of the fibres behaviour at the tip of the extrusion nozzle.

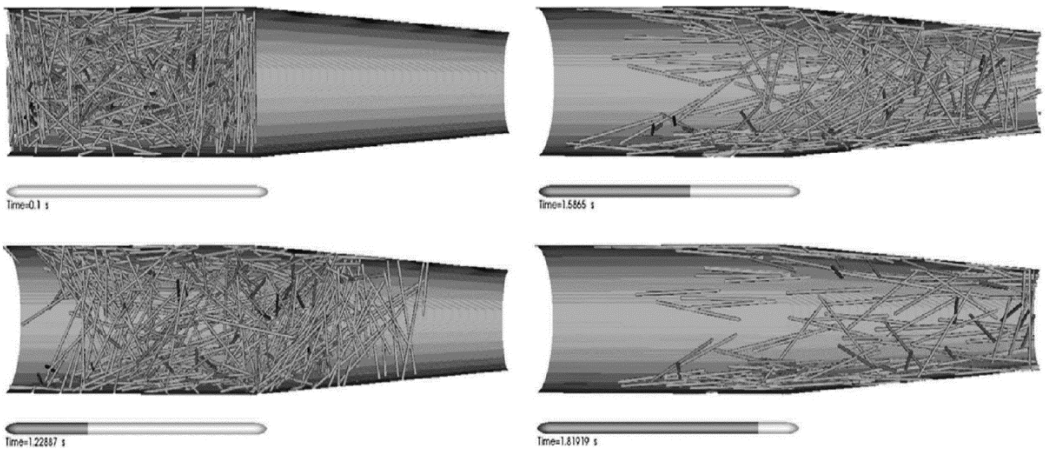

Figure 6 – Simulation of the fibre orientation evolution with time, at a constante pressure [7].

It was also reported in [8] that when deposed, the fibres tend to be located mainly in the surface of the filament. Furtherly, its presence also impacts the thermal properties of the deposed filament, and consequently, the thermal behaviour of the component. For this reason, it can be assumed that the solidification behaviour is, to some extent, different from the unreinforced counterparts, thus, it can be concluded that the inclusion of fibres has a significant impact on the bond formation process. It is then expected that final components reveal differences in terms of fracture toughness.

2.2 Target materials

As mentioned before, the materials applied in this dissertation were the polyamide 12 in its pure form and its reinforced version, with short carbon fibres. This decision was made based on research requirements in this area, which is the implementation of reinforced composites in the FDM process [12], [13]. The materials which will be applied were obtained in its final form, ready to use, and were acquired from Fillamentum®, being the designated name for the pure form Nylon FX256, and for the reinforced version Nylon CF15 Carbon. The aspect of each type of filament is presented in Figure 7.

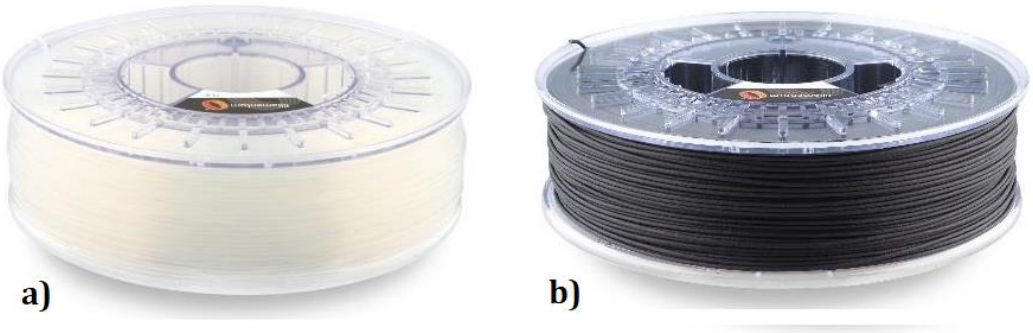

Figure 7 – Filaments used for the dissertation. a) Nylon FX256 [14], b) Nylon CF15 Carbon [15].

This type of polymer is widely regarded as an engineering plastic, being suitable for applications which require load bearing. The interest in applying this material to the FDM technology is understood as a need for further advancement in the mechanical properties, which are able to be obtained from it. Furthermore, the same type of investigations is also currently being conducted for other engineering plastics, for instance ABS [16], [17] and PLA [18], which reinforces the appropriateness of searching a method suitable for this one.

2.2.1 Problems of the FDM process

In the light of the explained concepts in section 2.1.2, it is important to refer that the conclusions obtained, while affecting the FDM process of every material employed, also do so in different ways, due to the inherent properties of each one. In fact, in the current moment, the research done in this area reports that the inclusion of fibres can result in both positive and negative effects on the outcome of the component's mechanical properties [19], depending on the type of interface created between the matrix and the fibre. For the composite parts to have increased mechanical properties, the load transfer between the matrix and the reinforcement must also be ensured. If the created interface reveals itself as weak, the component can exhibit reduced mechanical properties, even if every aspect mentioned in section 2.1.2 is correctly addressed [20].

In fact, the linking between the two components of the material also holds a significant influence on the outcome of the final part. Regarding the reinforcement applied, short carbon fibre, a few considerations must be taken into account, which are related to the scope of this dissertation. Various authors have classified the wettability of this type of fibre as poor. In result of this, the adhesion to the matrix polymer is prone to exhibit a poor behaviour as well [21]. For the polymer which will be employed in this dissertation, however, different studies report that the inclusion of this type of fibre reveals itself as beneficial to overall properties of the final composite material [22], [23]. From these observations, the reinforced material properties can be expected to be greater in comparison with the pure counterparts. Special treatments can be made in order to increase the wettability of this type of fibre [24], however, the reinforced material data sheet applied in this dissertation does not refer to any specific treatment.

The polymer employed in this dissertation has had its behaviour extensively studied for the creation of components. A property which is referred as transversal to all the variances of this polymer is its hygroscopic behaviour, both from water and the moisture presented in the air [25]. The same studies report that the moisture negatively influences the mechanical properties of the polymer. This effect can also be linked to the adhesion strength in the composite case, as shown in [26], which states that not only the increasing content of moisture can have harmful effects on the mechanical properties of the matrix, it can also attack the interface between matrix and fibre, possibly causing its debonding. From the points stated, it

can be furtherly assumed that this is another variable, which has to be taken into account, when analysing the data obtained from the experimental test.

2.3 Fracture mechanics concepts

Due to being created with a layer by layer step process, the parts obtained from the FDM technology can be regarded in the same light as laminate composites. In result of this, they tend to exhibit the same type of problems as these composites. Among them, the possible delamination effect between adjacent plies is one of the most severe that can occur, being its consequence a reduction on the mechanical properties, resulting in an early failure of the component [13]. This effect is due to a crack propagation phenomenon, which is a typical application of the fracture mechanics concepts. The same problems are prone to occur between adjacent layers of the FDM components, since the process itself is responsible for the separation of the layers, as it is evidenced by Figure 8.

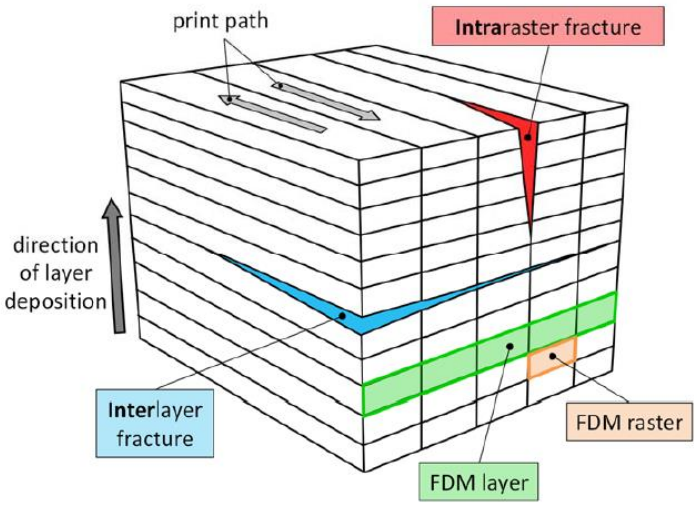

Figure 8 – Common types of fracture in FDM manufactured components [20].

For this reason, it was assumed as adequate to make use of these concepts to analyse the interlaminar fracture in these parts, which is a conclusion also stated in [27]. For the fracture process, the crack propagation behaviour can be described in three distinct modes, as seen in Figure 9.

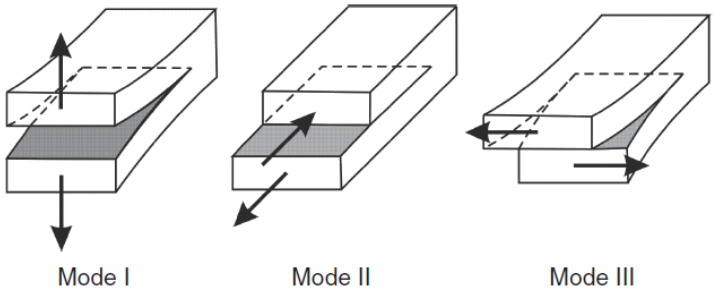

Figure 9 – Loading fracture modes [28].

This dissertation will be focused in describing the behaviour of the components for the mode I propagation. This decision is because both the technology and materials applied for the manufacturing of the experimental specimens are still in a relatively initial phase of development, being that no values are reported for the specific combination applied. In addition, the layer by layer configuration gives rise to critical interfaces that can contain defects influencing interlaminar fracture under mode I loading.

The method followed for this analysis can be based on two different approaches, differing for the type of material it is employed. It is to be remembered, from section 2.1.2, that the connection between adjacent layers can be described as a set of linking points. For this reason, both types of material used for this dissertation can be considered as heterogeneous. Thus, an analysis which takes into account stress intensity points is not advisable, since it is susceptible to errors induced by variations in adjacent zones of the material. Consequently, the energetic concepts were the criteria chosen to follow, as they are capable of estimating the global fracture parameters of the material. In doing so, they transmit a better idea of the fracture process itself [28]. This type of concept was firstly introduced in [29], which reported that crack propagation occurs when the energy available at the crack tip reaches a certain value, G_C, which is the critical strain energy release rate. This value is an inherent property of each material and the fundamental parameter which is aimed to be obtained in this dissertation. The following relation can be established to define the strain energy release rate (G):

$$G = \frac{dW}{dA} - \frac{dU}{dA} \tag{2.1}$$

where W is the work performed by an external loading, U is the strain energy of the body, and dA is the variation of cracked area. Considering a general body with width B, loaded on the direction perpendicular to the cracked area, the work done by the external load can then be described as $W = P\delta$, while elastic the strain energy can be defined by $U = (1/2)P\delta$ where P and δ are the applied load and resulting displacement, respectively. Combining these equations,

and considering the current compliance of the body $C = \delta/P$, the Irwin-Kies relation can be obtained,

$$G = \frac{P^2}{2B}\frac{dC}{da} \tag{2.2}$$

with *da* being the variation of the crack length. As it is perceived by the inclusion of this parameter, the values obtained for G correspond to the critical energy release rate during propagation. This equation is of great importance for the experimental work, as it is the base fundament from which the estimation of this parameter is obtained.

2.3.1 Experimental process

As stated in section 2.3, the focus of this dissertation was to describe the fracture propagation behaviour, specifically for the failure under mode I loading. The standardized test for this mode is the Double Cantilever Beam (DCB) test [30]. In this procedure, a pre-cracked specimen is loaded under the conditions shown in the first Figure 9, in order to promote a pure mode I opening. The displacement-loading rate is defined previously, and is constant throughout the duration of the test, normally with a range of values of 1-5 mm/min. The load is applied using piano hinges or load blocks, as shown in Figure 10.

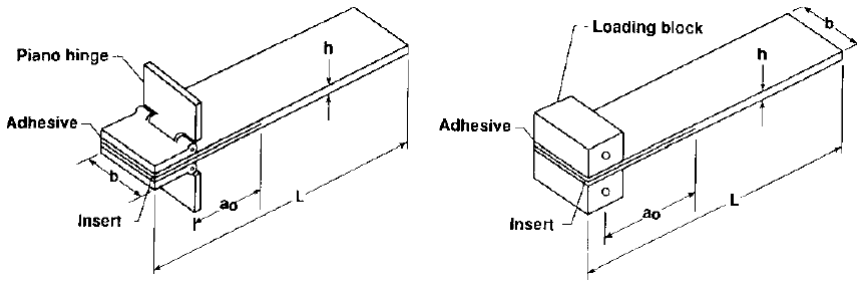

Figure 10 – Schematic representation of the DCB test [30].

The set of data usually obtained from this standard test consists of the load *P*, the correspondent applied displacement δ, and the observed crack length *a*, which are measured with a specified frequency, usually 1-5 Hz. By recording these values throughout the duration of the test, the fracture energy for mode I can be estimated, using appropriate data reduction schemes. It is important to refer the different types of reduction schemes, which can be applied for this estimation, in order to decide the most adequate for this specific case. Most frequently, the data reduction scheme applied are the Compliance Calibration Method (CCM), and the

Modified Beam Theory (MBT), being both tests procedure standardized in [30]. The first requires the definition of a function $C = f(a)$ that fits the recorded experimental values, which is then used to calculate the parameter dC / da presented in the Irwin-Kies relation (equation 2.2). In the MBT, a new concept is introduced in order to account for the crack tip rotation and deflection, being this value determined via compliance function, this time generated through linear regression analysis. The issue with the referred data reduction schemes is the need for a record of the crack length through the duration of the test, which is sometimes hard to perform due to the material behaviour. In fact, the measurement of this parameter is prone to induce errors in the fracture energy analysis.

Taking into account the nature of the technology and materials applied for this dissertation, another data reduction scheme will be applied, the Compliance-based Beam method (CBBM). This data reduction scheme has the advantage of not relying on the crack length measurement, by the introduction of a new concept, the equivalent crack length. This value accounts for a fracture process zone (FPZ) which develops at the crack tip and cannot be accurately measured, being explained in more detail in section 3.2.2.

2.4 Advances in the technology

As observed earlier, the addressed subjects for this dissertation are relatively recent. Consequently, a test method which can be described as universal is yet to be implemented, for the type of technology and materials involved. Furtherly analysing what has been researched in this area, there are a few common points which can be regarded as the first steps to a standardized test mode. In [20] for instance, a similar study as this dissertation is conducted, for the ABS polymer. In this paper, a modified version of the ASTM D5528 is applied for the experimental tests, followed by the use of the CCM data reduction scheme. The authors concluded that this standard is an adequate way to characterize the interlayer performance of FDM components, and that its association with material characterization tests may prove critical for the development of this technology. Furtherly sustaining this conclusion, a study presented in [31] attempted to characterize the fracture behaviour of DCB specimens created with ABS, employing cohesive damage models. The authors concluded that this type of approach can be used as an effective tool to capture the interlayer fracture behaviour of the FDM components, as well as to improve the fracture energy estimation procedure of the final components. It is important to refer that this type of approach will also be applied in this dissertation, in an attempt to confirm its use as an adequate method for the estimation of the material's cohesive parameters. This analysis will be explained in more detail in chapter 4. Lastly, in [5], a DCB test is conducted on samples manufactured with PLA, another engineering plastic. In this paper, the authors conclude that the layer design parameters, such as its thickness or raster orientation specific for the type of load applied, are key aspects in enhancing the interlaminar strength of the final component. They also stated that the DCB test is appropriate to perform studies for this type of technology.

3 Experimental work

3.1 Specimen development

3.1.1 Imposed conditions and geometry dimensioning

As a first approach, the specimen dimension procedure applied in [20] was considered. In this paper, the authors decided, due to the low stiffness of the material (ABS), to apply glass/epoxy doublers as a way to prevent the deflection of the specimens during the DCB test. While this can be an effective method of reducing the deflection, it can also increase the overall fracture toughness of the specimen, since when solicited, the interface between the doublers and the specimens can also absorb fracture energy, which is difficult to keep account. Even if this type of over estimation can be made negligible considering the use of a strong adhesive, it must be taken into account that there is no reference for the expected fracture toughness values of the specimens, which makes difficult the assessment of the relevance of spurious energy being dissipated. For these reasons, another path was followed based on dimensioning of specimens taking into consideration the low Young modulus of the material. The bending stiffness ($E_1 I$) imposed for the specimen's arms was based on previous works ([5], [32]) using DCB tests which have pointed to values of the order of $10^6\ Nmm^2$. Another condition was imposed, which was the specimen standards for the dimensioning presented in [30]. For the materials used, Nylon FX256 (PA12) and Nylon CF15 Carbon (PA12+sCF), the mechanical property values were obtained from previously performed tensile tests on specimens created by the same process (FDM), at INEGI. The Young modulus found for PA12 was 1565 MPa, and for the PA12+sCF, 1907 MPa. From the array of combinations obtained, the decision on the final dimensions was also made based on the possible warping effect which can take place due to the thermal gradient induced by the continuous deposing of filament. The defined specimen dimensions were then obtained, being presented in Table 2.

Table 2 – Defined specimen dimension for each type of material.

Specimen Material	Length *L* [mm]	Width *B* [mm]	Height *h* [mm]	E_1 [MPa]	*I* [mm^4]	E_1 **I* [Nmm^2]
PA12+sCF	125	25	6	1907	450	8.58E05
PA12	125	25	6	1565	450	7.04E05

As already referred, the determined bending stiffness refers to each arm of the specimen (Figure 11), which means that each specimen has a total height of 12 mm (6 mm each arm).

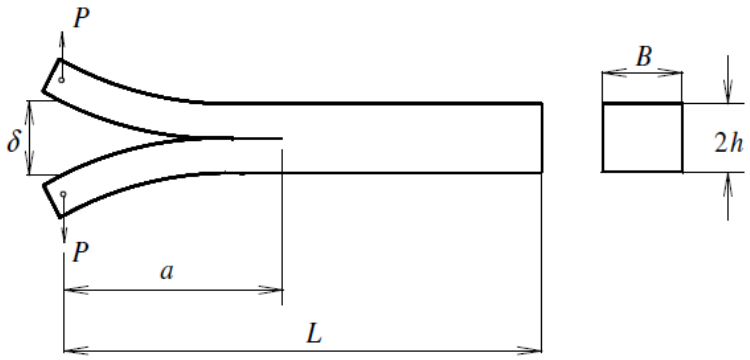

Figure 11 – Schematic representation of the DCB test [33].

3.1.2 Specimen 3D modelling

After the dimensioning, the specimens were created using SolidWorks 2017®, with dimensions as according to the ones presented in Table 2. The pre-crack was introduced in the specimens by applying a Kapton film insert during the FDM printing process, in a similar way as seen in [20]. This procedure required several steps in order to allow the accurate printing of the specimen dimensions, being explained in more detail in section 3.1.3. The resulting file was exported to .STL format, in order to be processed by Simplify3D®, which, as seen in section 2.1, renders the 3D model obtained into code instructions for the printer to apply. This software also gives the ability for the user to freely modify all the variables presented in the FDM process, as well as an estimation of the time needed to print the specimen.

One of the many options available for modification within the software is the infill percentage, which plays an important role on how the crack propagation occurs, due to its influence on the bending stiffness and toughness of the created specimen. A lower infill results in a non-solid cross-section, as seen in Figure 12, which negatively affects the value of the second moment of area *I*, since less material is deposed.

Figure 12 – Aspect of a 40% infill rate specimen. The black arrows indicate void zones within the specimen.

In Table 3, a comparison between a commonly used infill rate in FDM (40%), and the applied in this experimental work (100%) is presented. The Young modulus of the 40% infill rate specimen was considered to be around 60% of the 100% infill rate specimen, in order to adjust this value to account for the effect mentioned earlier (the decrease in I [mm^4]). This assumption was made based on the results presented by [34], which reported this relation between infill rates.

Table 3 – Comparison between two different infill rates.

INFILL RATE	SPECIMEN	Apparent E_1 [MPa]	Adjusted E_1 [MPa]	$E_1 * I$ [Nmm^2]	Variation
40%	**PA12**	1565	939	4.23E+05	2.82E+05
	PA12+sCF	1907	1 144	5.15E+05	3.43E+05
100%	**PA12**	1565	-	7.04E+05	-
	PA12+sCF	1907	-	8.58E+05	-

This difference can be mitigated by increasing the dimensions (height and width), of the 40% infill rate specimen. However, since the use of a lower infill would result in having a non-solid cross-section, the 100% infill rate was chosen as the path to follow, as it is the rate that ensures the least possible amount of air gaps and voids between the deposed layers.

With this choice and the specimen dimensioning completed, the information obtained was inputted into the software, which allows it to then estimate the time needed for completion of the print, the filament length used, and the weight of the specimen. A 3D preview of the specimen in which the number of layers needed and the option to observe a specific one is also presented. Figure 13 illustrates what was explained before.

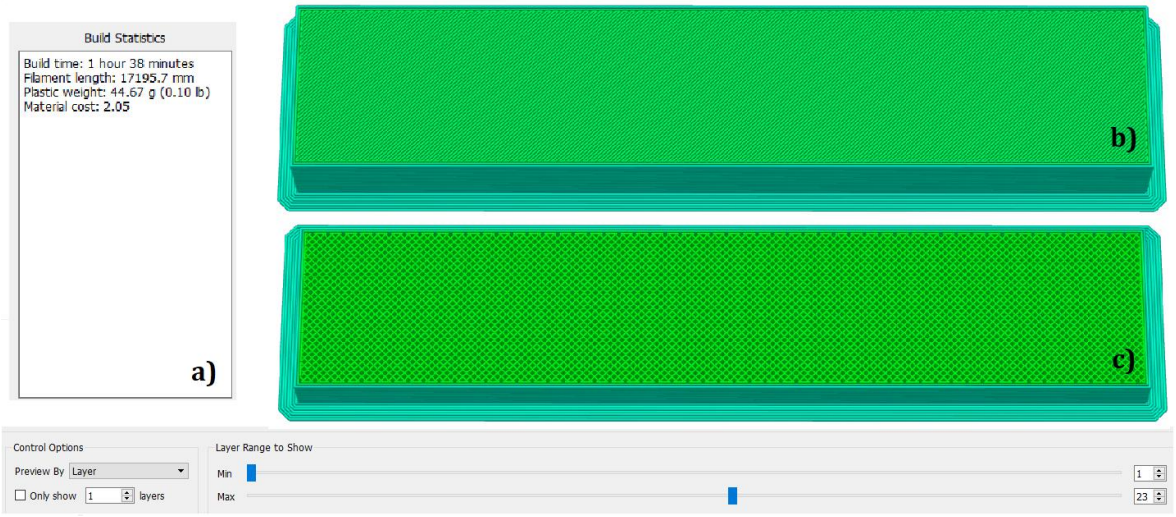

Figure 13 – Information obtained from the process preview. a) Build statistics. b) Complete specimen. c) Cross-sectioned specimen.

The software then creates the G-code file, which acts as a set of instructions for the printing path, while carrying the information concerning the infill percentage and printing specifications such as the ones presented in the Table 4. This file was then loaded into the 3D printer, in order to create the specimen. The printer model used for this experimental work was the commercially available Tronxy X5, illustrated in Figure 14.

Table 4 – FDM parameters used for the DCB specimens manufacture process.

Layer height [mm]	0.3
Top solid layers	2
Bottom solid layers	2
Outline/perimeter shells	2
Number of layers	40
Printing speed [mm/s]	60
Infill rate [%]	100
Infill orientation [º]	45/-45
Print bed temperature [ºC]	90
Extrusion nozzle temperature [ºC]	260

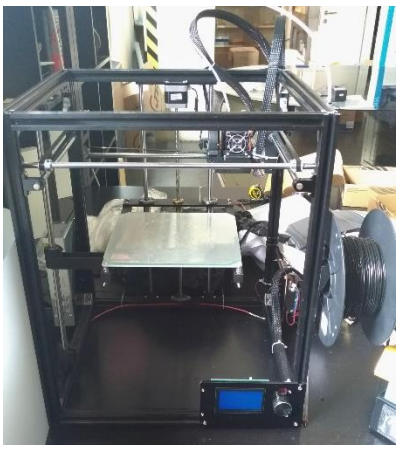

Figure 14 –Tronxy X5 3D printer applied on the manufacturing process.

3.1.3 Specimen printing method

As mentioned earlier in this chapter, a specific method was developed in order to allow the creation of specimens, which could then be evaluated through the DCB test. The later was a result of the experience gathered along the process of learning and correcting the imperfections of each specimen, which were caused mainly by the high infill rate chosen. The FDM process is not generally used with such high percentages; however, this was the path to follow, since the DCB test requires a stable crack propagation rate in order to be successful, which is achieved by ensuring the least amount of voids and gaps within the specimen.

As a consequence of the high infill percentage applied, the filament length deposited in each layer and the time needed to complete it also increases. This heavily influences the thermal gradient of the specimen, leading to a higher warping effect as the temperature of the layers created previously tends to bed temperature (90ºC), and the filament is extruded from the nozzle at 260ºC. The resulting thermal contractions, in addition to deformation of the specimen themselves, also contribute to small dimensional errors. In fact, the position of the newly deposited layers by the nozzle will be influenced by the previous ones, which results in the specimen not having a perfectly vertical cross section [10]. In order to reduce the warping effect described here, a thin layer of 3D systems Cube glue® was applied to the print bed prior to printing, to promote the adhesion of the first layer of extruded filament.

In addition to this problem, another issue was found while printing the specimens, being it when creating the pre-crack during the printing. Following the procedure carried out by [20], a Kapton film was applied between the layers adjacent to the mid-plane of specimen. Being the specified height for each layer of the specimen 0.3 mm, the specimen then contains 40 separate layers, corresponding to its total height of 12 mm, which means the film is applied between the 20^{th} and 21^{st} layers. However, due to poor adhesion between the layers and the film, this process was not straightforward, and required several tests in order to be able to insert the Kapton film without affecting the printing of the specimen. The results of the first attempts at printing are shown in Figure 15, Figure 16 and Figure 17, being both the issues described earlier illustrated by them.

In Figure 15, the thermal contraction effect mentioned earlier can be observed, mainly in the edges of the specimen. A solution to this problem was found, which was increasing the area of contact between the specimen and the heated bed, in order to counteract the warping effect.

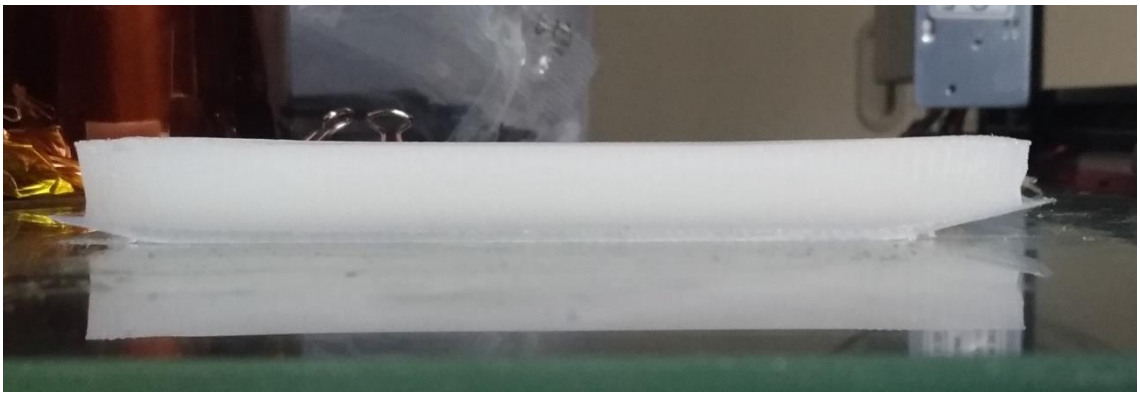

Figure 15 – PA12 specimen with warped edges, resulting from the thermal contraction effect.

In Figure 16, the first attempt at inserting the pre-crack is presented. As it can be observed, the Kapton film did not adhere correctly to the bottom layer. After the deposition of the 21st layer, both layer and film started to warp, causing the specimen's pre-crack to be defective thus not able to be tested.

Figure 16 – Warping effect in the 21st layer.

Afterwards, in order to solve this problem, the film was applied in a different way, as seen in Figure 17 a). The followed strategy consisted in fixing the support where the film is taped thus impeding its warp. However, due to the inexistence of adhesion between the newly deposed layer and the film, this layer started to warp right after being deposed. Another type of film was also used, being this the Blue painter's tape, to find out if the resulting pre-crack had a better quality. As it can be seen by Figure 17 b), the use of a different type of tape showed similar results as the Kapton film mentioned earlier, with the first layer deposed after the placement of the tape not adhering correctly, thus, it was concluded that this was not the path to follow.

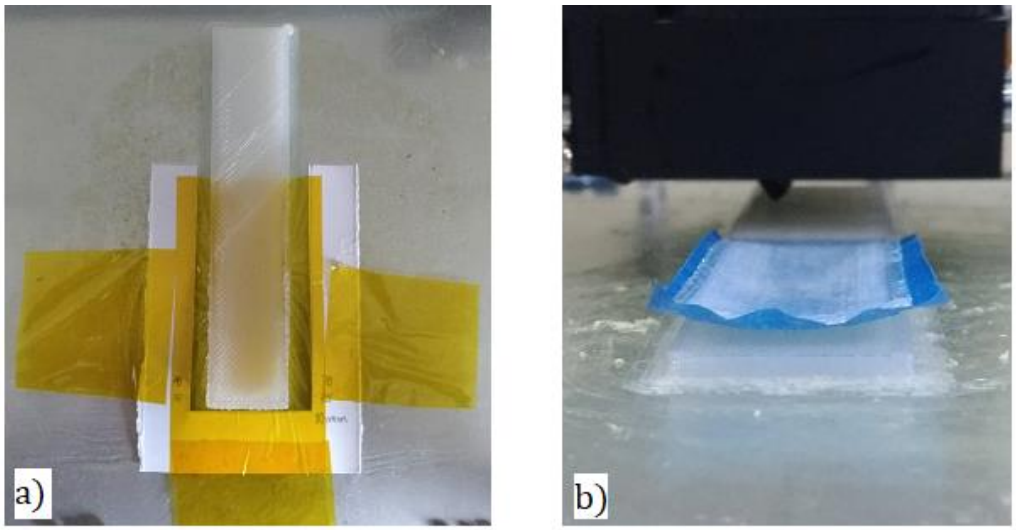

Figure 17 – Attempted approaches for a solution to the warping effect. a) With Kapton film. b) With Blue painter´s tape.

Since neither of the approaches used worked correctly, a new geometry was created, containing a part solely for support, which was used to prevent the film and specimen from warping, by depositing 2 extra layers on top of the film. Also, as mentioned before, the increase in area adhering to the heated bed is also beneficial since it counteracts the thermal contraction effect. The appearance of the new geometry is shown on Figure 18, and it consists in three different parts combined.

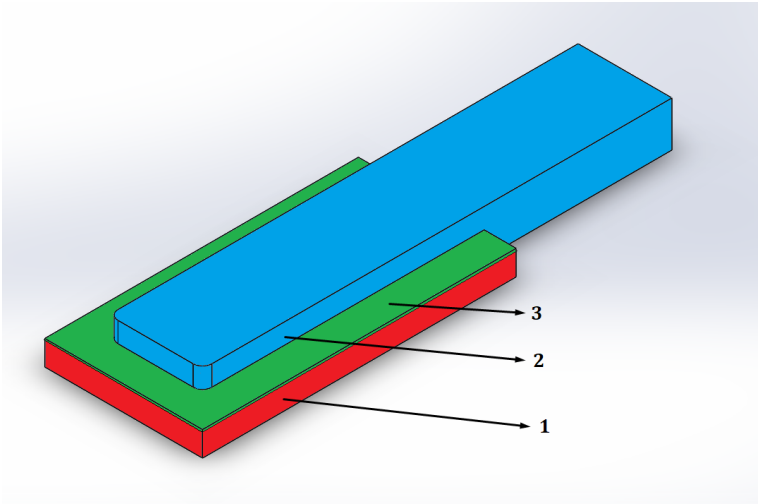

Figure 18 – Three-dimensional CAD model designed for the new geometry approach. 1- Support, 2- Specimen, 3- Enclosing layers.

The printing starts with parts number 1 and 2, as seen in Figure 19 a). Both are printed until reaching the height of 6 mm, and at this point the print is paused and the Kapton film is applied in order to create the pre-crack (see Figure 19 b).

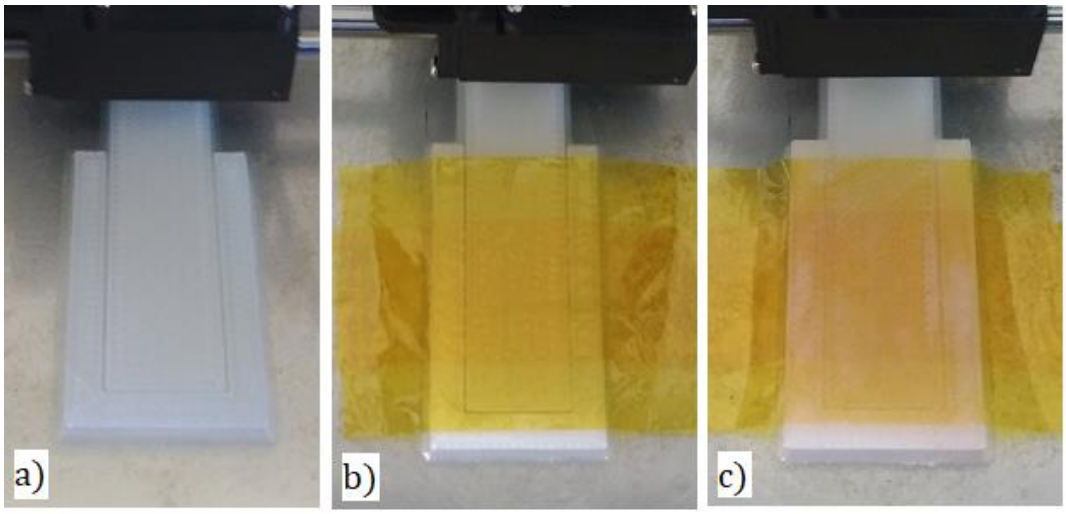

Figure 19 – Main stages of the new geometry approach: a) Support and specimen are printed till 6 mm height. b) Kapton film is applied. c) Entrapment of the Kapton film.

Afterwards, part 3, which is a rectangle with the same length and width of the support, and 2 layers worth of height (0.6 mm), is printed on top of parts 1 and 2. This allows the Kapton film to be sealed, while also preventing the layers deposed on top of it from warping, since part 3 also adheres to a part of the support which is not covered by the Kapton film. After the printing, the resulting part is taken out of the bed, and the support and film are cut out, resulting in a specimen as seen in Figure 20.

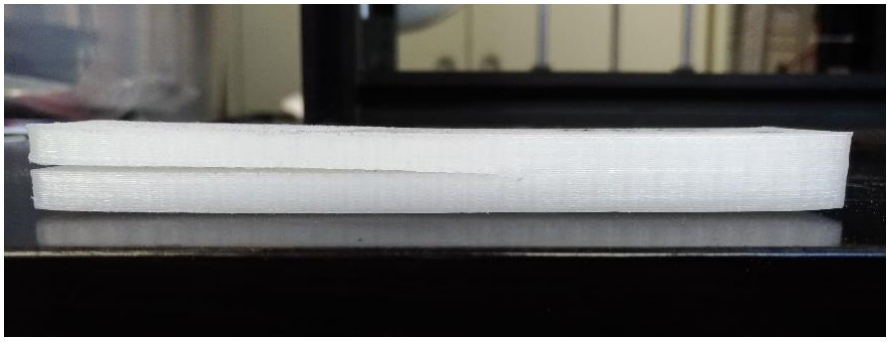

Figure 20 – Resulting PA12 specimen from the new approach followed.

3.1.4 First results

The above described approach was followed to produce specimens with accurate dimensions, since the warping effect described earlier is controlled as it can be seen in Figure 20. Each specimen took approximately 2 hours and 30 minutes to be created. In Table 5, the dimensions of the created specimens are presented.

Table 5 – Dimensions obtained for the first series of specimens.

SPECIMEN	Length L [mm]	Width B [mm]	Height h [mm]	Pre-crack a_0[mm]
PA12-1	123.95	25.16	5.43	46.8
PA12-2	123.36	25.12	5.51	46.3
PA12-3	123.9	25.17	5.38	47.2
PA12-4	124.48	25.17	5.57	47.4
Average	123.92	25.16	5.47	46.93
Deviation [%]	-0.86	0.62	-8.8	-6.14
PA12+sCF-1	125.08	25.83	5.58	46
PA12+sCF-2	125.9	25.62	5.67	47.13
Average	125.49	25.73	5.63	46.56
Deviation [%]	0.39	2.9	-6.25	-6.9

Although minimized, the warping effects were not completely removed mainly due to the high infill percentage. In fact, the dimensions obtained show a slight deviation from the intended ones, which causes the 3D printer to make small dimensional errors throughout the printing process. However, since this variable (the high infill percentage) is necessary to the experimental work, the only option is to try to control the printing process, which was what was done before. Since the warping effect could not be completely eliminated, the height presented in the table was measured in six different points of the arms zone, for each one, since they are the parts under stress of the specimen. Afterwards, an average value was considered to be used in the numeric analysis in order to minimize the effect of differences in height caused by the warping effect, as seen in Figure 21.

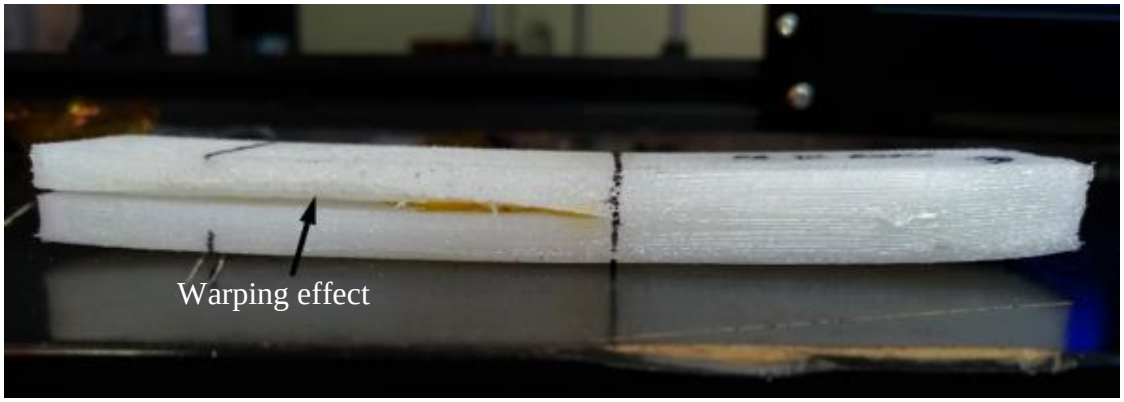

Figure 21 – PA12 specimen obtained from the first series. The black arrow confirms the presence of warping effect in the specimen's arm.

3.1.5 Cure process

Two piano hinges were bonded to the end of each specimen, as shown in Figure 22, following the procedure presented in the [30]. Prior to bonding, the surfaces of the hinges and the specimens were polished with sandpaper and cleaned with isopropyl alcohol, to ensure the load transfer without debonding. After the adhesive was applied, a peg was placed in each specimen, as seen in Figure 22, to prevent the hinges from moving and to ensure an optimal cure process of the adhesive, which lasted two days.

Figure 22 – Cure process of the specimens.

The last column of the Table 5 refers to the pre-crack length obtained, which was measured after the process described earlier was concluded, being it the distance between the hinge and the end of the pre-crack (the black line drawn in the specimen in Figure 22).

3.2 DCB test

After the completion of the cure process, the specimens were tested at INEGI's facilities, in the laboratory of mechanical testing using an Instron Model 4208 universal testing machine with 5kN load capacity and an opening rate of 5 mm/min.

3.2.1 Experimental remarks

In Figure 23, the beginning and end of the DCB test are presented, for one of the PA12 specimens. Crack propagation at the pre-cracked plane was able to be achieved, hence it can be concluded that the dimensioned geometry worked correctly.

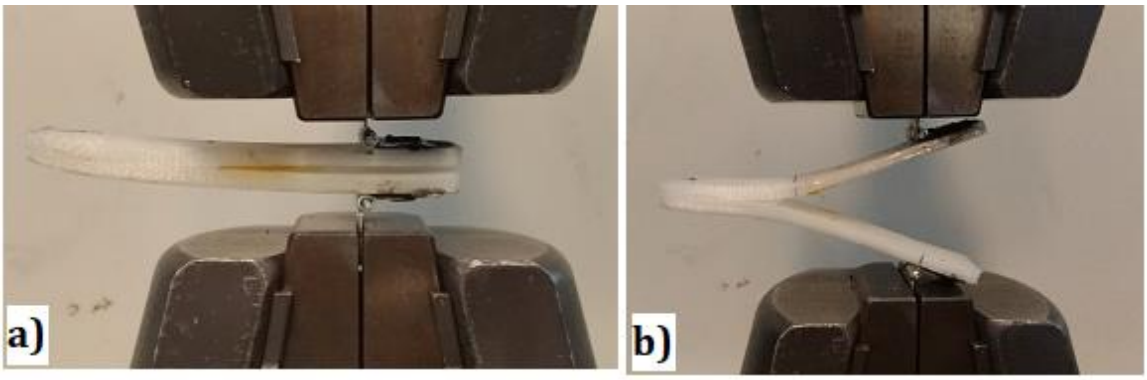

Figure 23 – First series DCB test for a PA12 specimen. a) Initial position. b) End position.

In Figure 24, a PA12+sCF specimen DCB test is presented. In this case, crack propagation at the pre-cracked plane was also achieved. However, a difference in flexibility can be noticed when comparing both specimens at end position. Since the dimensions are equal, this is due to the difference in the Young modulus, which is higher in the reinforced specimen leading to greater bending stiffness.

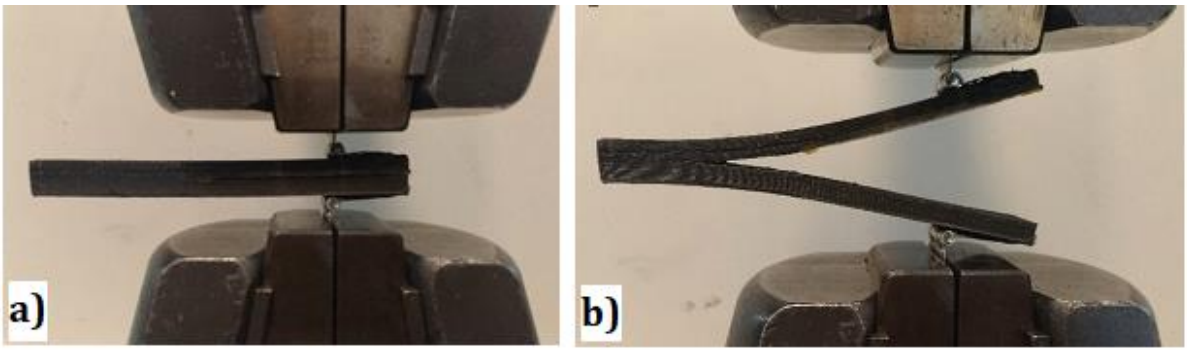

Figure 24 – First series DCB test for a PA12+sCF specimen. a) Initial position. b) End position.

All the specimens present in Table 5 revealed a steady crack propagation, except the specimens number 1 and 3 of the unreinforced material. The reason attributed to this behaviour is the defective height value found for these two specimens, which, as observed, correspond to the most deviated values. For each specimen, the machine recorded a set of data containing the applied displacement (δ) and the resulting load (P), i.e. the load-displacement curve.

3.2.2 Compliance-based beam method (CBBM)

The resulting data provided by the Instron universal machine was then analysed through the CBBM, being this method chosen because it allows the estimation of an equivalent crack length (a_e) throughout the experimental test without requiring its measurement. This is particularly advantageous since crack length monitoring is difficult to be performed with the required accuracy and accounts indirectly by the energy dissipated in the fracture process zone (FPZ) [33]. The FPZ is the region ahead of the crack tip where several mechanisms of energy dissipation coalesce, as presented in Figure 25.

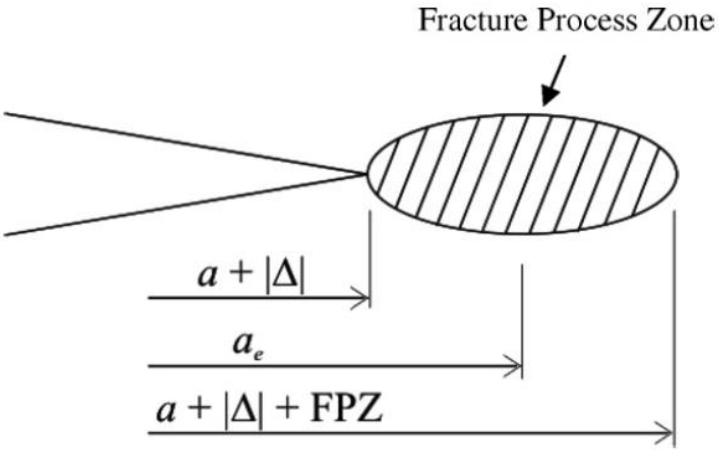

Figure 25 – Schematic representation of the FPZ and equivalent crack length concept [33].

Applying the Timoshenko beam theory [32], the specimen compliance *C* can be expressed as

$$C = \frac{8a^3}{E_1 B h^3} + \frac{12a}{5BhG_{\mathrm{LR}}} \tag{3.1}$$

This equation can be solved in order to *a* aiming to get the equivalent crack length a_e as a function of the current compliance, *C*. The solution of this cubic equation is obtained using the Matlab® software, as seen in [28], [33]. Thus, combining the Irwin-Kies equation (2.2) with equation 3.1, the expression obtained for strain energy release rate becomes,

$$G_I = \frac{6P^2}{B^2 h}\left(\frac{2a_{\mathrm{e}}^2}{h^2 E_{\mathrm{f}}} + \frac{1}{5G_{\mathrm{LR}}}\right) \tag{3.2}$$

Following this procedure, an estimation of the mode I energy release rate G_I as a function of compliance obtained experimentally can be made, for each moment in the test, thus, the *Resistance*-curve (*R*-curve) can be obtained. The only issues faced when applying this data reduction scheme were the values used for E_f, the corrected Young modulus, and G_{LR}, the shear modulus, which were not available. The corrected Young modulus was determined by an inverse procedure fitting the initial stiffness of the numerical load-displacement curve to the experimental observed one. In order to get accurate values, each specimen was simulated considering its real dimensions instead of the nominal ones. In the case of the shear modulus, it can be observed from equation 3.2 that it's importance is low when regarding the overall result. Consequently, a value was assumed for it, considering that in a generic orthotropic material, the shear modulus is typically 10 times lower than the Young modulus, for the referred direction.

This data reduction method revealed itself suitable for this type of material, since as it will be seen later in chapter 5, the crack propagation mode was not always stable, thus hard to measure in real time.

3.3 Second series of tests

Having the first estimation concluded, the next step was to furtherly investigate the reliability of these results, since data was only able to be obtained from two specimens of each material. In order to do this, three new specimens of each material were fabricated with the same dimensions, while applying the same procedure, and the data analysed, to corroborate the values obtained earlier. In Table 6, the measured dimensions of each specimen are presented, for the second campaign.

Table 6 – Dimensions obtained for the second series of specimens.

SPECIMEN	Length L [mm]	Width B [mm]	Height h [mm]	Pre-crack a_0 [mm]
PA12-1	123.9	25.18	5.21	48.9
PA12-2	123.7	25.65	5.17	49.3
PA12-3	124.1	25.6	5.23	49.02
Average	123.9	25.48	5.2	49.07
Deviation [%]	-0.88	1.92	-13.33	-1.86
PA12+sCF-1	125.32	25.75	5.23	48.59
PA12+sCF-2	124.9	25.80	5.19	49.31
PA12+sCF-3	125.3	25.83	5.13	50.08
Average	125.17	25.79	5.18	49.33
Deviation [%]	0.136	3.16	-13.67	-1.34

The values obtained mainly present differences in terms of height, when comparing to Table 5. It should be remembered, from the second moment of area ($Bh^3/12$), that the height of the arm has a heavy influence on the bending stiffness of the specimen, and consequently, on the successfulness of the test. Taking this factor into account, a DCB test end position is shown for each type of material, in Figure 26.

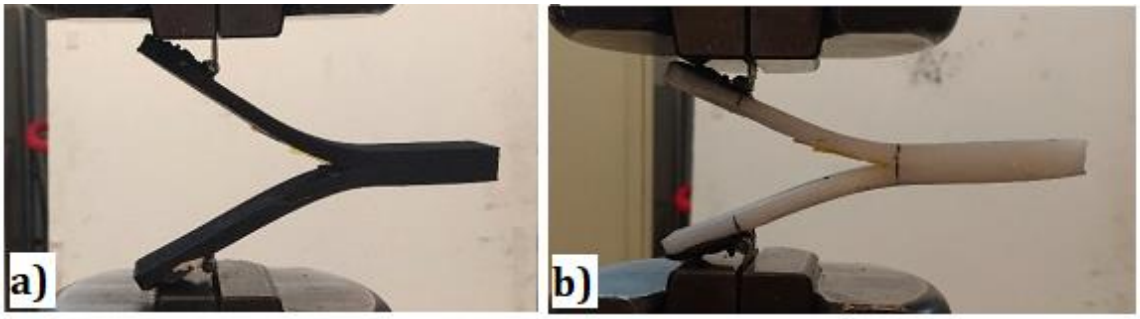

Figure 26 – Second series DCB test end position. a) PA12+sCF specimen. b) PA12 specimen.

As it can be verified, crack propagation did not occur in any of the specimens presented, being that the test ended when the tip of the specimen's arm touched the machine, as noticed in Figure 26. Furthermore, the same behaviour was registered in all the other specimens. It can be concluded that the created specimens did not have the sufficient bending stiffness in order for the pre-crack to propagate. As it was referred earlier, the measured dimensions indicated smaller values in terms of height when comparing to the previous series, which in turn negatively affected the second moment of area value of each specimen arm. In addition, the time in between printing and testing of the specimens was longer in this case (10 days). Since the conditioning of the specimens was not taken into account, the material mechanical properties may have decayed, because polyamide is a thermoplastic prone to suffer from hygrothermal degradation [35]. Consequently, no valid results were able to be retrieved from this batch of specimens. In an attempt to explain the behaviour exhibited by the specimens, the correspondent bending stiffness value for each one is presented in table 7. For this calculation, the initial estimated Young Modulus (1565 MPa for PA12, 1907 MPa for PA12+sCF) was applied, in order to obtain a comparison with the initially imposed value (10^6 Nmm^2).

Table 7 – Comparison of the obtained bending stiffness with the initially imposed values for the dimensioning.

SPECIMEN	**PA12-1**	**PA12-2**	**PA12-3**	**PA12+sCF-1**	**PA12+sCF-2**	**PA12+sCF-3**
***E*$_1$*I [Nmm^2]**	4.64E+05	4.62E+05	4.78E+05	5.69E+05	5.87E+05	5.54E+05
Variation [%]	-53.6	-53.8	-52.2	-43.1	-41.3	-44.6

As observed, the bending stiffness value of the specimens was significantly lower in comparison with the previous batch, or the imposed value whatsoever, and so, it was concluded

that this was the cause for unsuccessful tests. After the completion of this batch of specimens, the nozzle of the 3D printer had to be changed due to being clogged, which could have been the reason for the lack of height noticed in all of the specimens.

3.4 Third series of tests

Since no conclusion regarding the first estimation could be obtained from the previous batch of specimens, another iteration was made, while this time considering the problems faced previously. In order to solve the bending stiffness issue, a new geometry was considered, in which the pre-crack value and total length were decreased, from 50 to 40 mm, and from 125 to 115 mm, respectively. This ensured the successfulness of the DCB test, since by decreasing the length of the pre-crack, the specimen's arm becomes stiffer, thus allowing the crack to propagate. In addition, the conditioning of the specimens was taken into account this time, being that in the time in between the printing and testing, which was smaller, the specimens were stored in a temperature and moisture controlled environment, in order to prevent a possible degradation of the material properties. Apart from these two aspects, the same procedure used in the initial estimation was applied, and, after measuring, the following dimensions were obtained (Table 8).

Table 8 – Dimensions obtained for the third series of specimens.

SPECIMEN	Length L [mm]	Width B [mm]	Height h [mm]	Pre-crack a_0[mm]
PA12-1	114.24	25.47	5.36	37.02
PA12-2	114.54	25.39	5.19	37.75
PA12-3	114.01	25.68	5.54	37.46
Average	114.26	25.51	5.36	37.41
Deviation [%]	-0.64	2.04	-10.67	-6.48
PA12+sCF-1	114.91	25.78	5.58	37.55
PA12+sCF-2	114.53	25.65	5.61	37.67
PA12+sCF-3	115.47	25.71	5.51	37.21
Average	114.97	25.71	5.57	37.48
Deviation [%]	-0.03	2.84	-7.17	-6.3

The results indicate, in terms of height and width, a good correlation when comparing to the first series of specimens, which is favourable since crack propagation occurred for these values. This, in addition to the solutions implemented to account for the issues faced in the previous iteration, ensured the successfulness of the DCB test, as seen in Figure 27, which shows the end position for a specimen of each type of material.

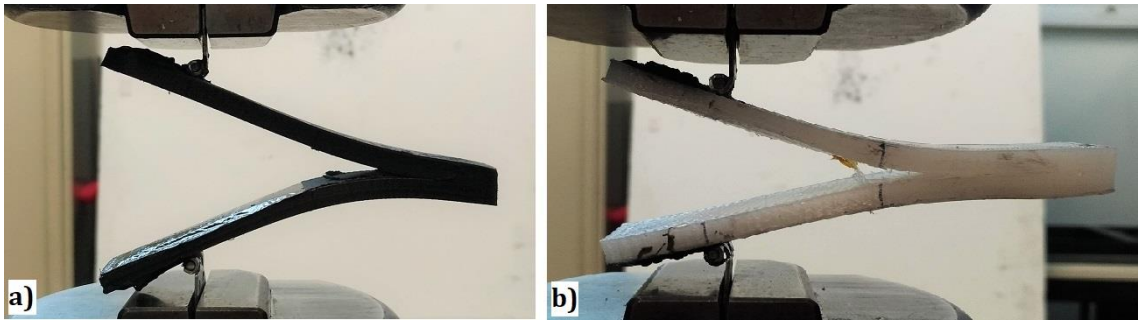

Figure 27 – Third series DCB test end position. a) PA12+sCF specimen. b) PA12 specimen.

With the completion of the DCB tests, the resulting information was analysed through the CBBM, in order to obtain the *R*-curve for each specimen. The aim here was to identify the value of the critical strain energy release rate, which is defined by the plateau on the *R*-curve, being it associated with the post-peak region of the *P*-δ curve. After the identification of the plateau in each specimen's *R*-curve, the experimental G_{Ic} values of each specimen were obtained. Since this series provided consistent values, the experimental work was then completed, being the next step the numerical analysis of the DCB tests.

4 Numerical analysis

4.1 Cohesive damage models

4.1.1 Trapezoidal law

As stated earlier, the next step was to verify the performance of the applied data reduction scheme, the CBBM. In order to do this, the DCB test was simulated numerically considering a trapezoidal cohesive damage model as a user subroutine implemented in ABAQUS® software. This model aims to simulate crack propagation in the DCB test, by placing interface finite elements where the damage is prone to occur [36], which in this case is the mid-plane of the specimen (Figure 28). The trapezoidal law was used due to some non-linearity observed in the load-displacement curve in the vicinity of the peak load. This behaviour is a symptom that some plasticity is associated to the fracture process, which is properly accounted for in the trapezoidal law.

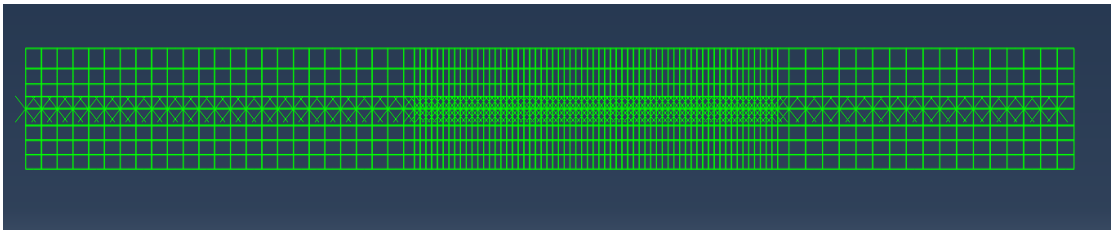

Figure 28 – Mesh applied for the numerical simulations. The crosses in the mid-plane indicate the cohesive elements.

The definition of the trapezoidal law requires five parameters: the experimental G_{Ic} value obtained for each specimen acting as the area of the trapezoidal law, σ_{U}, the local cohesive strength, $\delta_{1,\mathrm{I}}$, the relative displacement for damage onset, $\delta_{2,\mathrm{I}}$, the relative displacement defining the beginning of the stress softening part of the law and $\delta_{\mathrm{u,I}}$, which is the relative displacement that corresponds to complete failure of the bonding. These parameters, as seen in Figure 29, divide the behaviour of the specimen in three distinctive stages.

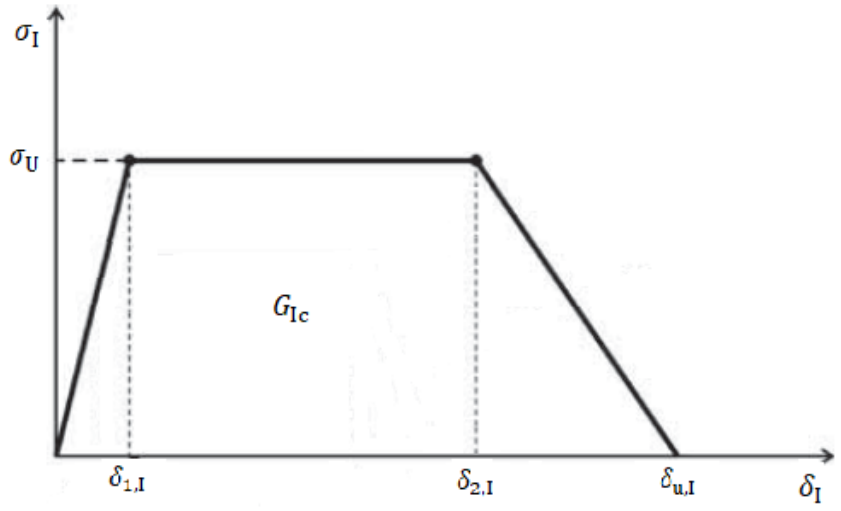

Figure 29 – Trapezoidal constitutive law for pure-mode I [36].

Until reaching the first inflexion point, defined by $(\delta_{1,I}, \sigma_U)$, before the occurrence of any damage, the model is in the linear elastic regime, being characterized by the following equation,

$$\boldsymbol{\sigma} = \mathbf{E}\boldsymbol{\delta}_\mathbf{r} \tag{4.1}$$

in which $\boldsymbol{\sigma}$ and $\boldsymbol{\delta}_\mathbf{r}$ are the stress and relative displacements vectors and **E** is a diagonal matrix containing the interface stiffness. The values inputted in this matrix aim to satisfy two requirements: first, the value should be as high as possible in order to minimize unwanted interpenetrations when compression occurs [31]; second, the value is limited in order to avoid numerical problems. These circumstances led to a compromise giving rise to a value normally in the range 10^6-10^7 [N/mm³], usually known as the penalty parameter.

After reaching the plateau, damage occurs, and the equation presented earlier turns into

$$\boldsymbol{\sigma} = (\mathbf{I} - \mathbf{D})\mathbf{E}\boldsymbol{\delta}_\mathbf{r} \tag{4.2}$$

where **I** is the identity matrix, and **D** is a diagonal matrix containing the damage parameter, d, for mode I, which can be calculated by

$$d = 1 - \frac{\delta_{1,I}}{\delta_I} \tag{4.3}$$

being $\delta_{1,\mathrm{I}}$ obtained from the local cohesive strength σ_{U} and the initial stiffness value. The size of the plateau is given by $\delta_{2,\mathrm{I}}$ and governs the plastic behaviour associated to fracture. After the second inflexion point $(\delta_{2,\mathrm{I}}, \sigma_{\mathrm{U}})$ a stress softening branch occurs, till complete failure when the relative displacement value $\delta_{\mathrm{u,I}}$ is reached. This value can be obtained from the following equation,

$$\delta_{\mathrm{u,I}} = \frac{2G_{\mathrm{Ic}}}{\sigma_{\mathrm{u,I}}} - \delta_{2,\mathrm{I}} + \delta_{1,\mathrm{I}} \tag{4.4}$$

As it can be noticed by the previous equations, the first three presented parameters $(G_{\mathrm{Ic}}, \sigma_{\mathrm{U}}, \delta_{2,\mathrm{I}})$ act as the imposed conditions. Considering the real dimensions obtained for each specimen, it is possible to determine the respective cohesive law by an inverse procedure. In fact, the cohesive law is iteratively adjusted aiming a good fitting between the numerical and experimental *P*-δ curves. When a good agreement is achieved, it can be settled that the cohesive properties applied are the ones that describe the material fracture behaviour. A numerical *R*-curve can also be obtained, in order to verify if the inputted G_{Ic} value is correctly reproduced by the numerical simulation.

After applying this model to the PA12 specimens, the same procedure was also conducted for the PA12+sCF counterparts. However, after simulating through the same cohesive damage model, it was verified that this law was not suitable for this type of material. In fact, it can be verified that the law could not reproduce accurately the early non-linearity arising before the peak load (see Figure 30).

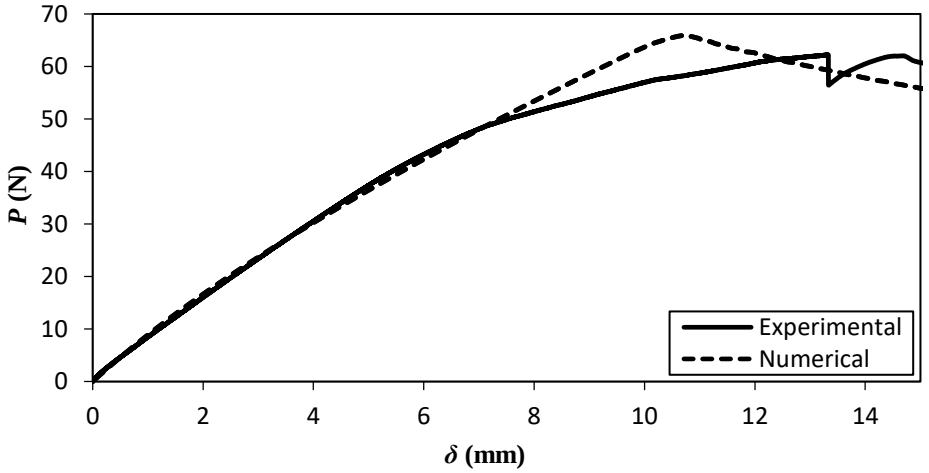

Figure 30 – *P*-δ curve comparison for the first series reinforced specimen (PA12+sCF) 1, applying the trapezoidal law.

4.1.2 Bilinear stress-softening law

In order to solve this incompatibility, another cohesive damage law was tested, since it was considered that it could be more suitable for this type of material. The bilinear stress-softening model distinguishes itself from the previous one, since, as it can be observed in Figure 31, the plateau which defines the second part of the behaviour does not exist. Instead, two different softening branches are used to describe different failure mechanisms. In result of this, the specimen's stiffness begins to decay earlier in comparison to the first model presented. This was the main reason behind this choice, since the numerical load-displacement curves obtained with the bilinear softening law are able to exhibit non-linearity earlier, as verified experimentally.

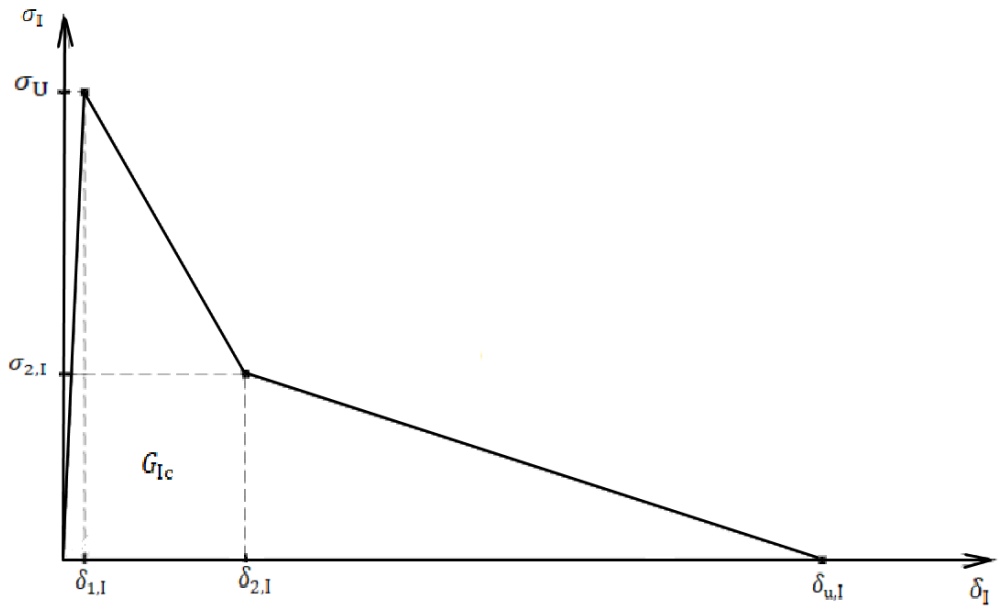

Figure 31 – Bilinear stress-softening constitutive law for pure-mode I [33].

The constitutive equation shown earlier (4.1) can also be applied until the first inflexion point ($\delta_{1,I}, \sigma_U$). From this point, the constitutive equation 4.2 is applied. However, two different slopes should be implemented to deal with different failure modes [33]. Thus, up to the second inflection point ($\delta_{2,I}$, $\sigma_{2,I}$) the damage parameter becomes,

$$d = \frac{\delta_{2,I}(\delta_I - \delta_{1,I})(1-\phi)}{\delta_I(\delta_{2,I} - \delta_{1,I})}, \quad \delta_{1,I} \leq \delta_I \leq \delta_{2,I} \tag{4.5}$$

being δ_{I} the current relative displacement and $\phi = (\sigma_{2,\mathrm{I}}.\delta_{1,\mathrm{I}})/(\sigma_{\mathrm{U}}.\delta_{2,\mathrm{I}})$. For the final branch and until reaching the ultimate displacement $\delta_{\mathrm{u,I}}$, the damage parameter is now calculated via the following equation,

$$d = 1 - \frac{\phi\delta_{2,\mathrm{I}}\left(\delta_{\mathrm{u,I}} - \delta_{\mathrm{I}}\right)}{\delta_{\mathrm{I}}\left(\delta_{\mathrm{u,I}} - \delta_{2,\mathrm{I}}\right)}, \quad \delta_{2,\mathrm{I}} \leq \delta_{\mathrm{I}} \leq \delta_{\mathrm{u,I}} \tag{4.6}$$

As seen by the previous equations, this model requires an additional parameter to be inputted ($\sigma_{2,\mathrm{I}}$), in order to fit the cohesive law to the experimental curve obtained. The defining values of this law are then σ_{U}, $\sigma_{2,\mathrm{I}}$, $\delta_{2,\mathrm{I}}$ and G_{Ic}, and, in fact, its implementation provided a better agreement between the experimental and numerical load-displacement curves, as it will be seen in chapter 5.

4.2 Finite element analysis

The models described earlier were then implemented as a user subroutine, in ABAQUS® software. The cohesive zone, where damage is prone to occur (the mid-plane of the specimen), was modelled by 106 8-node isoparametric plane elements, being the most part of these elements concentrated in the zone where crack propagation occurs, in order to obtain precise values for it. A plane strain state was assumed owing the width of the specimens (25 mm). The problem was then simplified to two dimensions, rendering it easier to process and more efficient time consuming. In Figure 32, the behaviour of the numerical simulation is presented, for the duration of test, along with the resulting numerical *P*-δ curve for the current displacement applied. Figure 32 a) shows the initial rising trend, before the peak-zone, which is displayed in b). Lastly, c) shows the post-peak region, in which a considerable amount of crack propagation can be perceived.

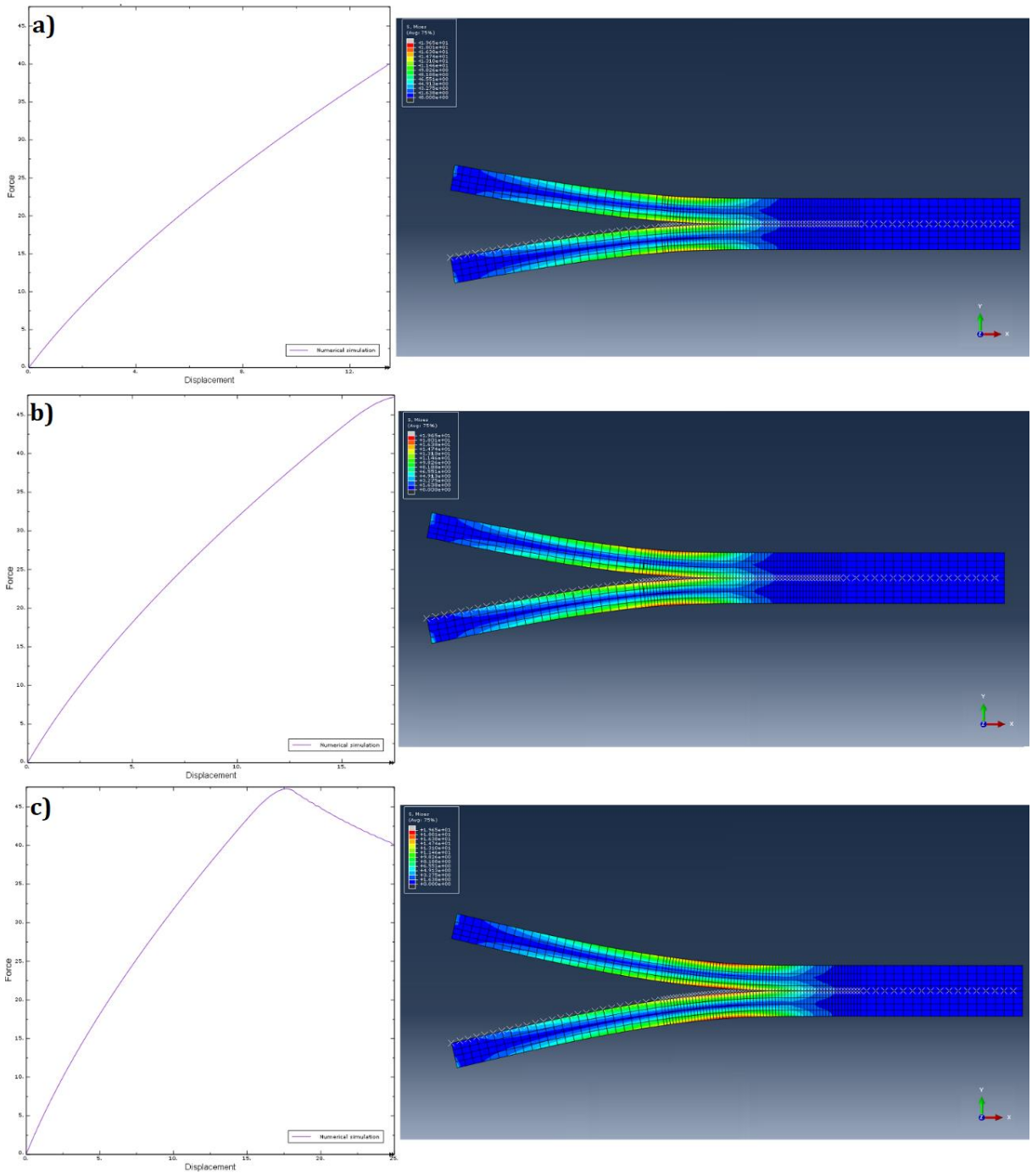

Figure 32 – *P-δ* curve and corresponding displacement of the numerical DCB specimen. a) Initial rising trend. b) Peak-zone. c) Post-peak zone.

5 Results and discussion

5.1 First series curve agreement

From Figure 33 to Figure 40, the resulting curve agreement obtained for the first series of specimens is presented.

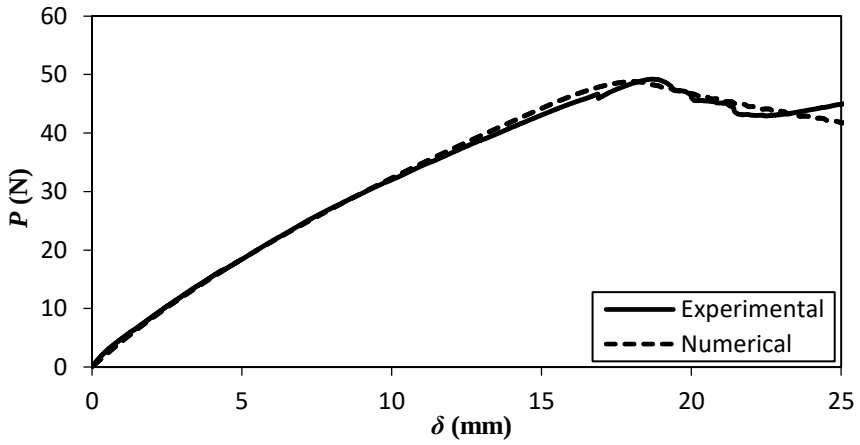

Figure 33 – *P*-δ curve comparison for the first series unreinforced specimen (PA12) 2.

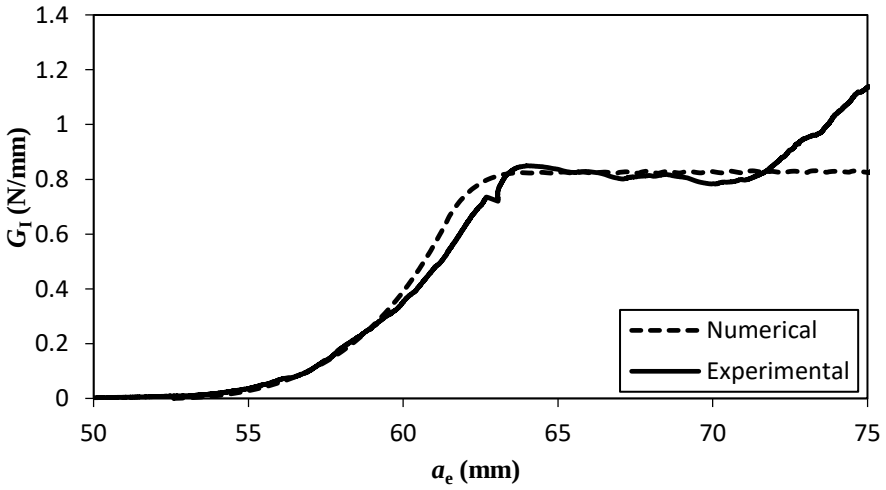

Figure 34 – *R*-curve comparison for the first series unreinforced specimen (PA12) 2.

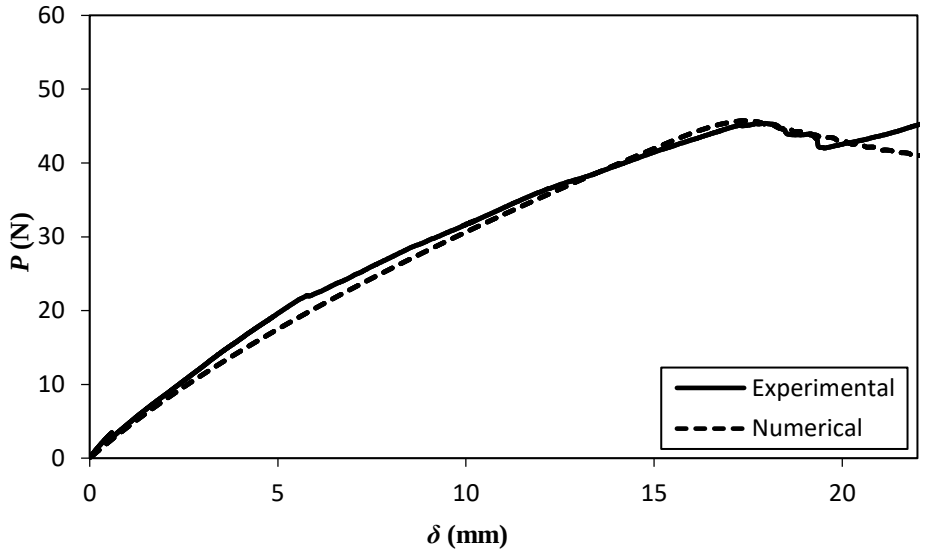

Figure 35 – *P*-δ curve comparison for the first series unreinforced specimen (PA12) 4.

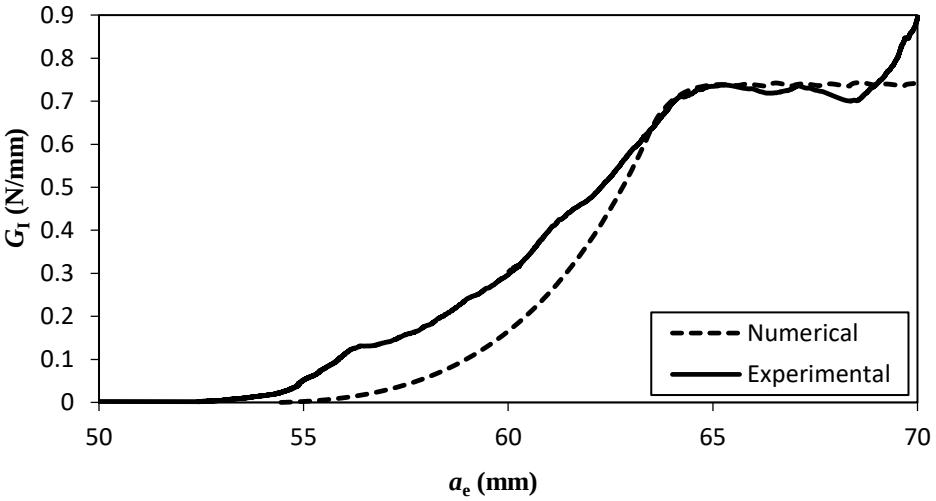

Figure 36 – *R*-curve comparison for the first series unreinforced specimen (PA12) 4.

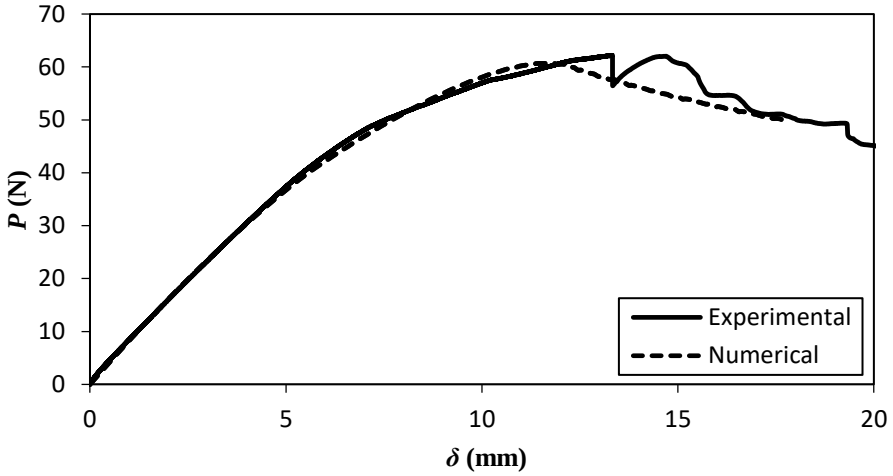

Figure 37 – *P*-δ curve comparison for the first series reinforced specimen (PA12+sCF) 1.

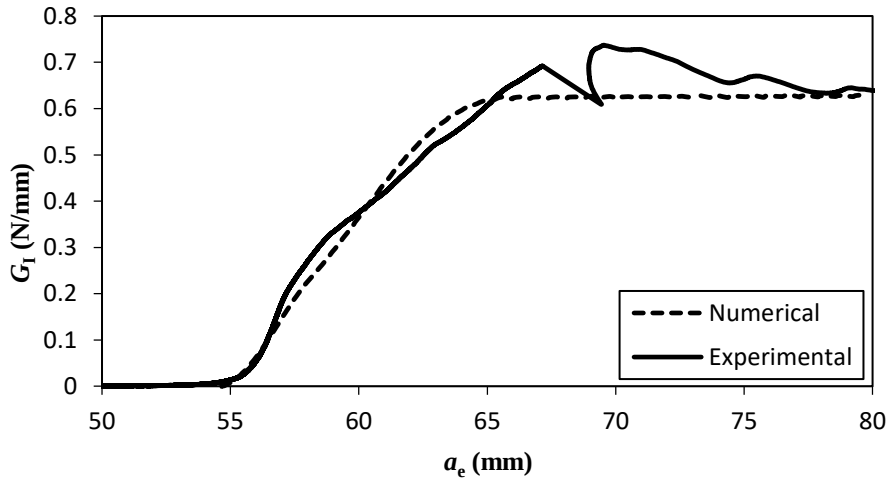

Figure 38 – *R*-curve comparison for the first series reinforced specimen (PA12+sCF) 1.

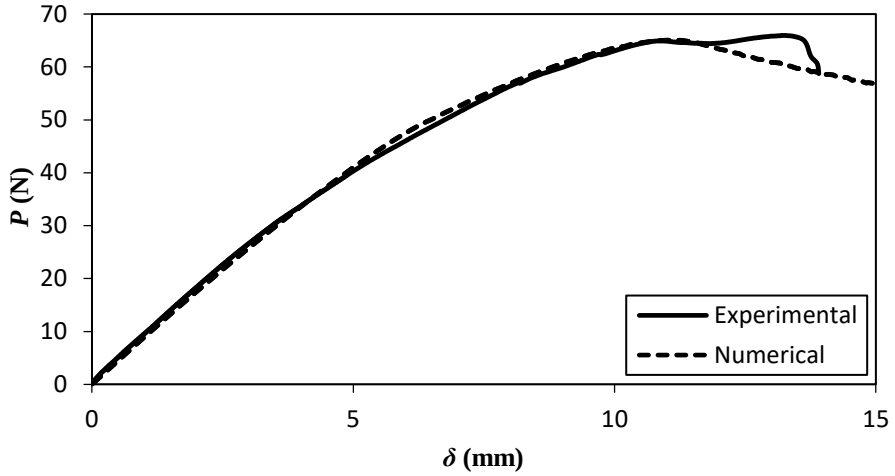

Figure 39 – *P*-δ curve comparison for the first series reinforced specimen (PA12+sCF) 2.

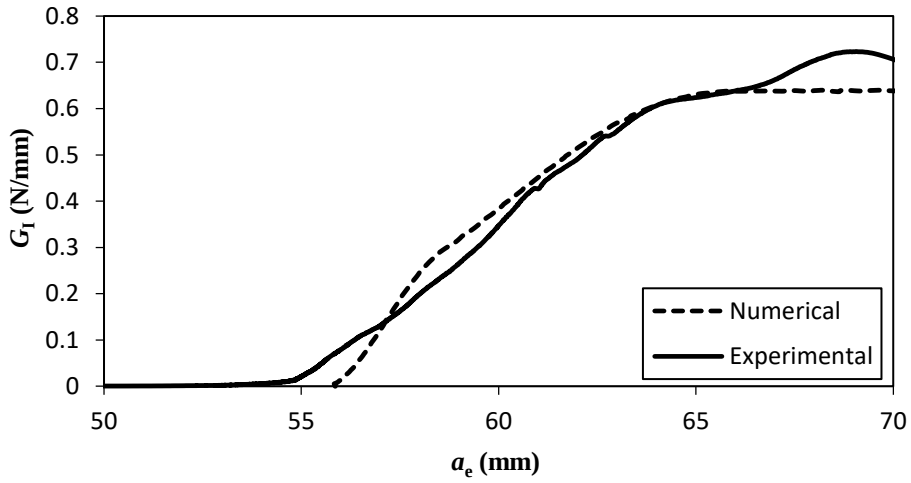

Figure 40 – *R*-curve comparison for the first series reinforced specimen (PA12+sCF) 2.

As it can be verified from the *R*-curves comparison, the identified G_{Ic} plateaus on the experimental curves are accurately reproduced by the numerical counterparts, in all cases. In addition to this, a good agreement could also be found between the *P*-δ curves, from which it can be concluded that the cohesive parameters that define the peak load zone (σ_{U}) and its curvilinear shape ($\delta_{2,\mathrm{I}}, \sigma_{2,\mathrm{I}}$ for PA12+sCF and $\delta_{2,\mathrm{I}}$ for PA12) are the ones that in fact describe the material's fracture behaviour. However, it can also be noticed that unlike the numerical curves, the experimental ones exhibit an irregular pattern, from which it can be perceived that the crack propagation did not occur in a steady way, in the majority of cases after the peak load zone. In fact, the influence of the last conclusion can also be denoted in the *R*-curves, and for this reason, the identification of the G_{Ic} plateaus required a post analysis of the resulting specimen surfaces, to determine the zones where the crack propagated correctly, and the reasons behind why it failed to. The method applied was to identify the critical cases, by observation of

the obtained curves, and, afterwards, gather information in order to correctly select the region where the plateau value is defined. It can be verified that for this series, the critical case was the PA12+sCF specimen 1. Its surfaces were then analysed in the microscopy at INEGI, being the results displayed in Figure 41.

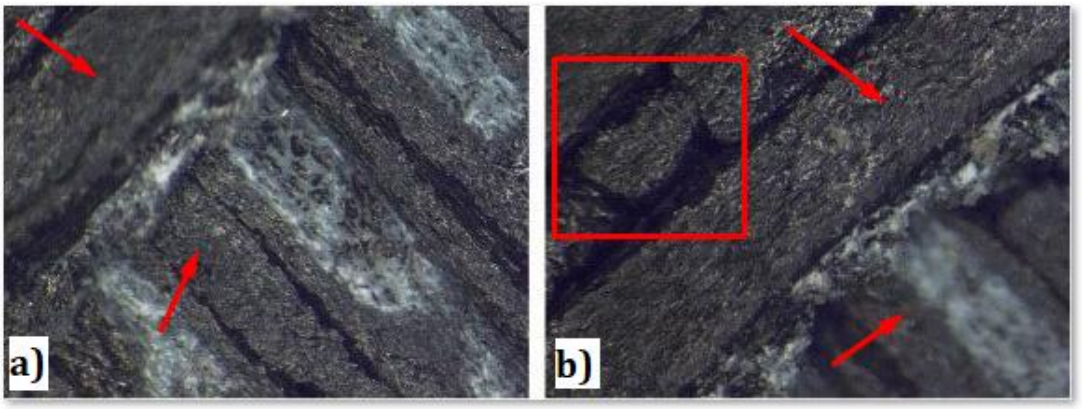

Figure 41 – Optical microscopy analysis. a) Focusing of the inferior layer. b) Focusing on the superior layer.

In this figure, the zone in which a layer pull out begins is shown in two different perspectives, as it is perceived by the different raster orientations (evidenced by the red arrows). For the perspective of the superior layer, b), a printing error can also be observed, since a difference in the amount of deposed filament can be perceived (as evidenced by the red rectangle). This effect, inherent to the production method applied (FDM), can also create differences in the interfacial adhesion between the deposed layers, thus, inducing variations in the load-displacement curve.

5.2 Third series curve agreement

From Figure 42 to Figure 53, the resulting curve agreement obtained for the third iteration is presented, following the same procedure applied on the first estimation. It is important to be reminded that, for this iteration, the specimen dimensions were altered, being the pre-crack (a_0) and total length (L) values decreased from 50 to 40 mm and from 125 to 115 mm, respectively.

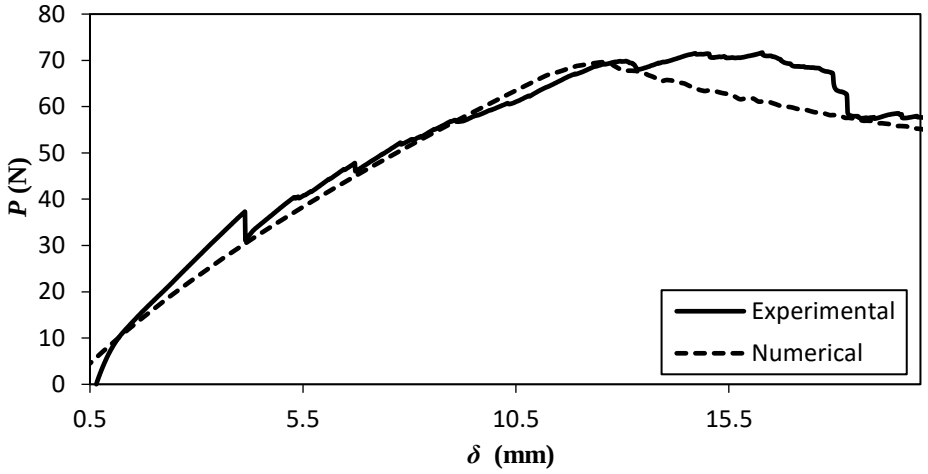

Figure 42 – *P*-δ curve comparison for the third series unreinforced specimen (PA12) 1.

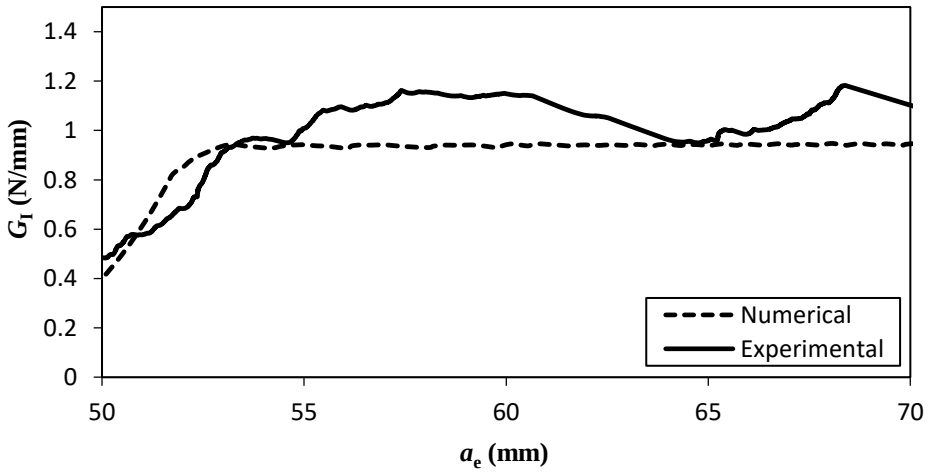

Figure 43 – *R*-curve comparison for the third series unreinforced specimen (PA12) 1.

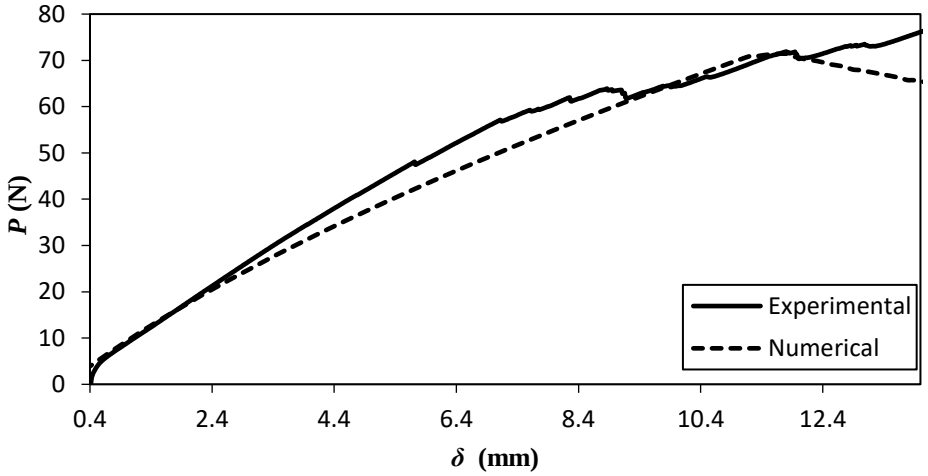

Figure 44 – *P*-δ curve comparison for the third series unreinforced specimen (PA12) 2.

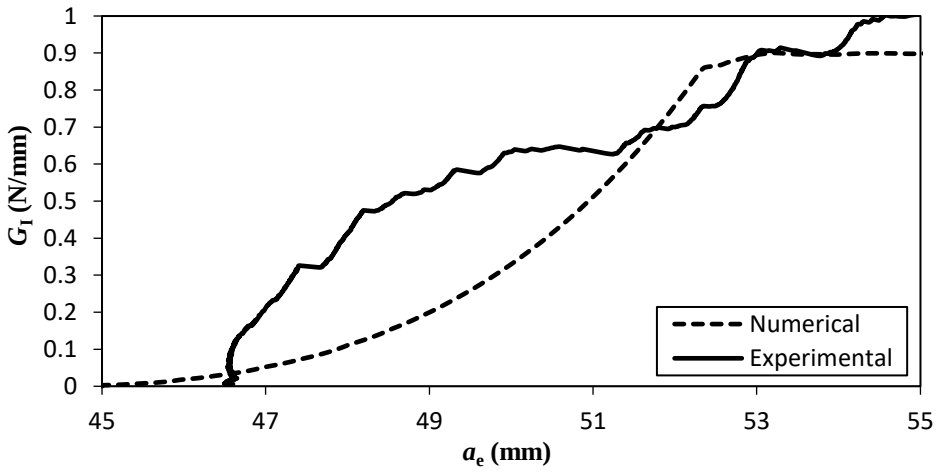

Figure 45 – *R*-curve comparison for the third series unreinforced specimen (PA12) 2.

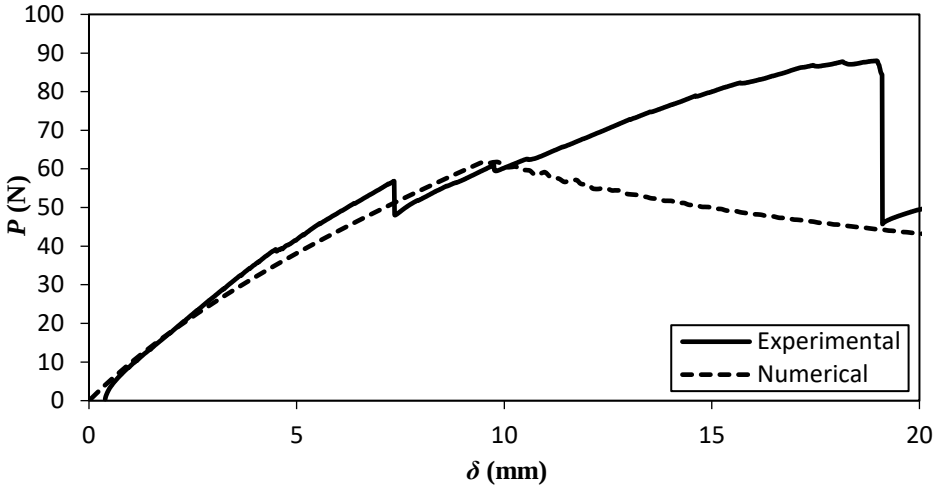

Figure 46 – *P*-δ curve comparison for the third series unreinforced specimen (PA12) 3.

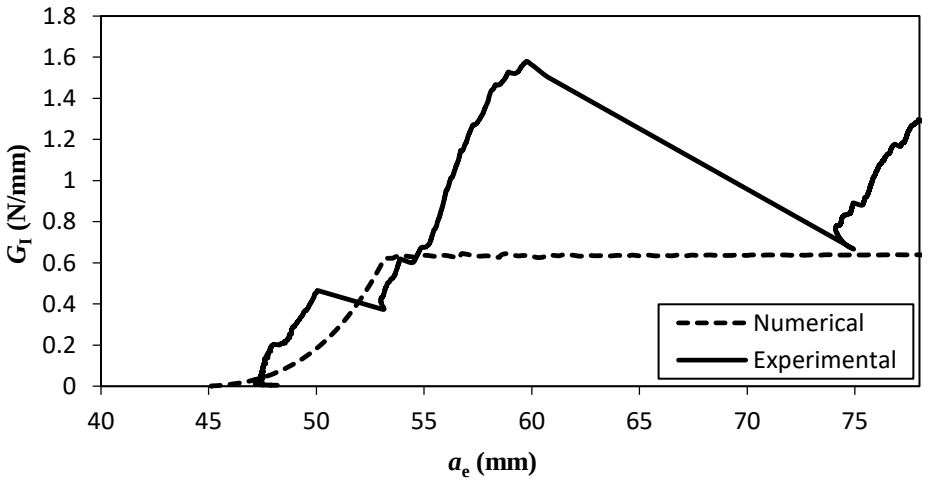

Figure 47 – *R*-curve comparison for the third series unreinforced specimen (PA12) 3.

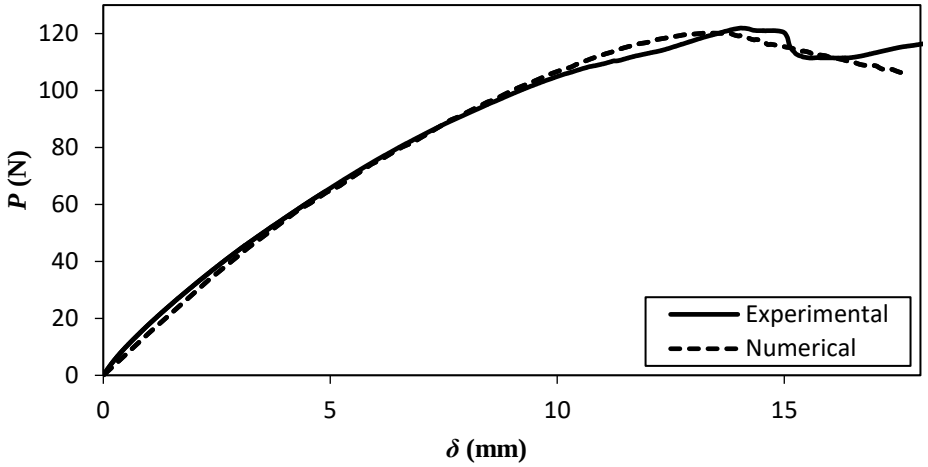

Figure 48 – *P*-δ curve comparison for the third series reinforced specimen (PA12+sCF) 1.

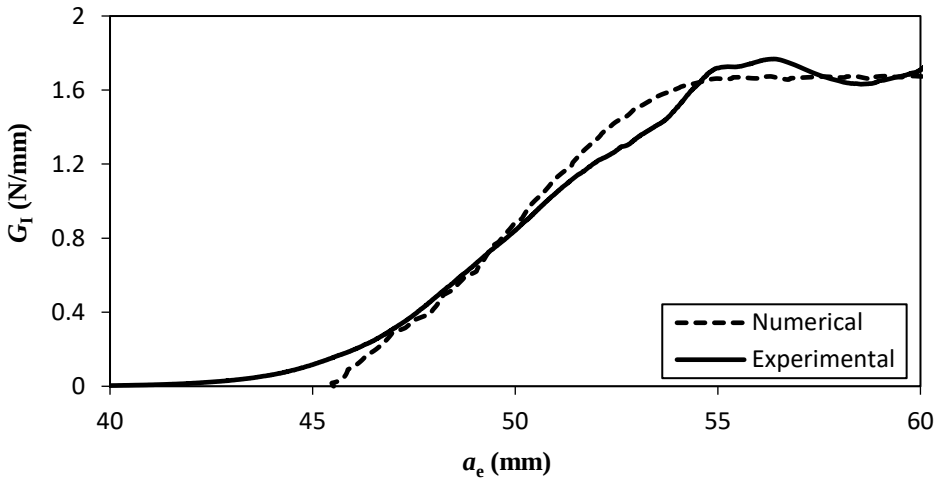

Figure 49 – *R*-curve comparison for the third series reinforced specimen (PA12+sCF) 1.

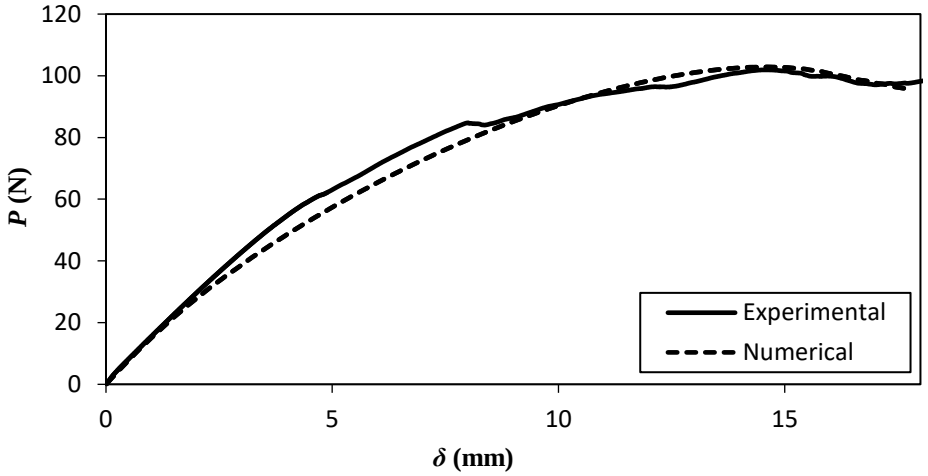

Figure 50 – *P*-δ curve comparison for the third series reinforced specimen (PA12+sCF) 2.

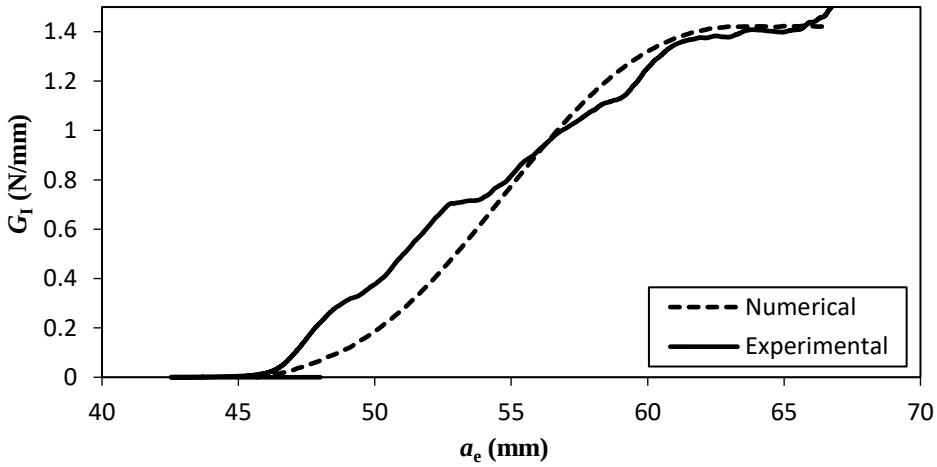

Figure 51 – *R*-curve comparison for the third series reinforced specimen (PA12+sCF) 2.

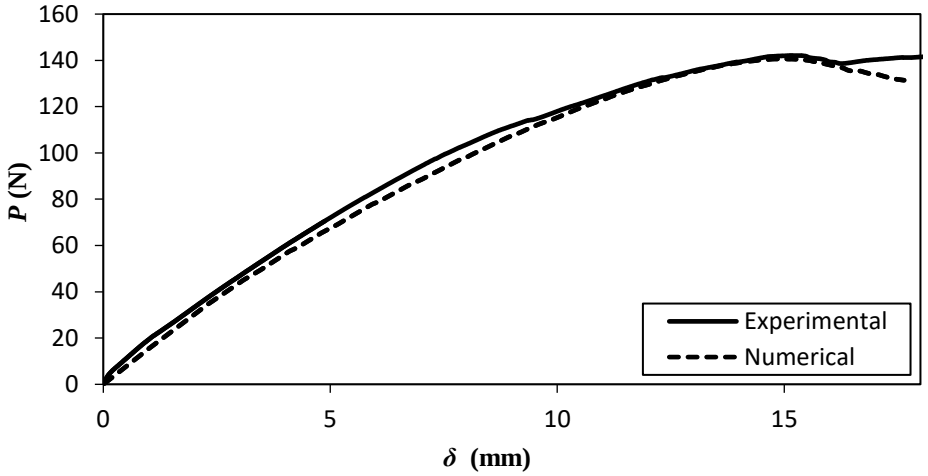

Figure 52 – *P*-δ curve comparison for the third series reinforced specimen (PA12+sCF) 3.

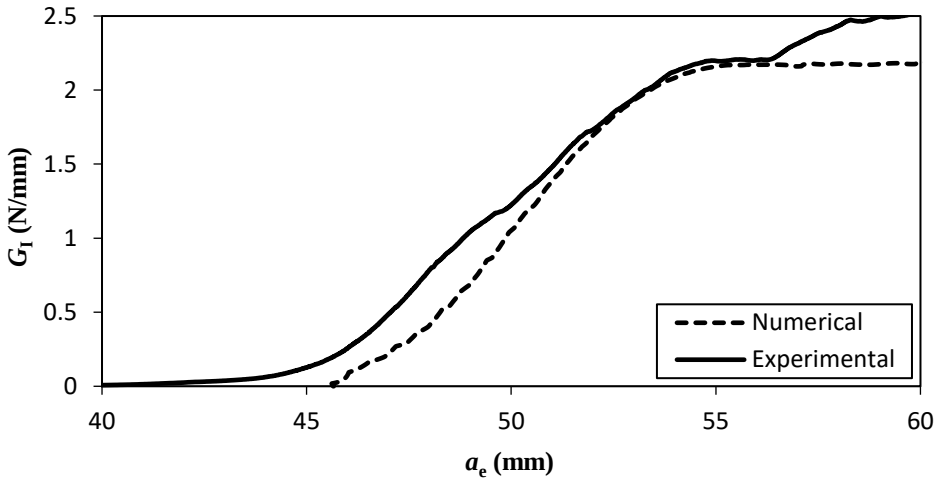

Figure 53 – *R*-curve comparison for the third series reinforced specimen (PA12+sCF) 3.

As it can be observed by the *P*-δ curves, the initial stiffness and peak load values obtained are higher in all the specimens, in comparison with the previous ones, which is a direct consequence of the length reduction performed in this iteration. The experimental *P*-δ curves obtained for the PA12 material also exhibit a highly irregular pattern, which difficult the identification of the G_{Ic} value since the data reduction scheme applied is directly dependent from the compliance. For this reason, the specimen surfaces required a post analysis in order to identify the regions where the crack propagated correctly.

An increase in the G_{Ic} value can also be observed in the PA12+sCF material, in comparison with the first estimation, which indicates that the conditioning settings applied for this batch of specimens positively influenced the mechanical properties of this material. However, this increase was rather slight in the PA12 material, which suggests that the higher

moisture weight presented in the first batch of specimens negatively affected the performance of the reinforced PA12, possibly weakening the interfacial adhesion between the short carbon fibre and polyamide. In fact, a slight increase in the G_{Ic} value obtained for the PA12 specimens was experienced, which corroborates the proposed conclusion, since this material also had its conditioning taken into account. This conclusion can also be perceived in [35], where the influence of the moisture is studied in polyamide 6, which is another variation of the material employed for this dissertation.

Lastly, two discrepant values can be observed in this series of specimens, being one in each type of material. The resulting specimen surfaces of the PA12 specimen 3 and PA12+sCF specimen 3 were then analysed, in order to understand the reason behind these values.

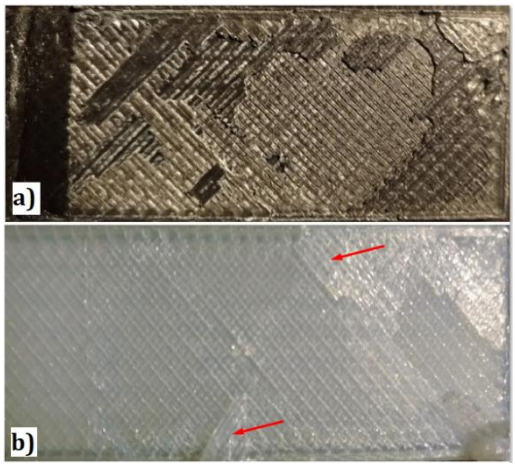

Figure 54 – Resulting surfaces after the DCB test. a) PA12+sCF specimen. b) PA12 specimen.

As it can be seen in Figure 54, both surfaces exhibit a layer pull out behaviour. As stated before, this made difficult the identification process of the G_{Ic} value, and may as well have influenced the value itself, since there is an additional force required in order to pull an extra layer of material. In the case of PA12+sCF specimen, this effect can justify the higher G_{Ic} value found, since it can be observed from the figure that the referred layer pull-out behaviour happened consecutively during the crack propagation, and in most of the cases, in one layer or more, simultaneously. As for the PA12 specimen, a pulled out layer in two different moments can be observed, but still attached to the surface (evidenced by the red arrows). This circumstance can justify the lower G_{Ic} value for this specimen, since it indicates a variation in interfacial adhesion between layers, in adjacent zones. This effect can be perceived by the abrupt variations on its both curves, being the G_{Ic} value found for this specimen the plateau for which the curve tended consecutively, after suffering the variations.

5.3 Obtained results

5.3.1 PA12 Specimens

With the completion of the curve analysis, each specimen values were then gathered in form of a table, in order to further investigate the obtained results. Table 9 contains the numerical inputted values for which the better curve agreement was achieved, for the PA12 specimens presented in sections 5.1 and 5.2.

Table 9 – Cohesive parameters obtained for the unreinforced specimens.

	SPECIMEN	σ_U [MPa]	$\delta_{2,I}$ [mm]	G_{Ic} [N/mm]	E_1 [MPa]	a_0 [mm]
1st TEST	PA12-2	0.475	1.35	0.815	1337	46.3
	PA12-4	0.45	1.375	0.725	1307	47.4
	Average	0.46	1.36	0.77	1322	46.85
3rd TEST	PA12-1	0.75	1	0.86	1777	37.02
	PA12-2	0.75	1.05	0.905	2178	37.75
	PA12-3	0.6	0.95	0.635	1904	37.46
	Average	0.7	1	0.8	1953	37.61
CoV [%]		23.81	17.63	13.75	22.05	-

In general, it can be observed that the specimens obtained for the third batch test exhibit a higher local cohesive strength (52%) and Young modulus (48%) when compared with the first series. This, in association with the lower relative displacement values also obtained for the third batch (-36%), suggests that there is a slight difference in the material's behaviour, as stated earlier in section 5.2. From the coefficient of variation (CoV) obtained for each parameter, it can be observed that the G_{Ic} variation (13.75%) is the lowest of all, thus, it can be concluded that the overall estimation of this parameter was successful, for this material. However, as it was already stated before, the specimen's geometry and conditioning were changed due to the conclusions drawn from the second batch of specimens. The new taken measures revealed themselves as beneficial for the material properties, and so, it can also be concluded that the material properties may be closer to the average values obtained for the third batch of specimens.

5.3.2 PA12+sCF Specimens

The obtained values for the first and third PA12+sCF specimens are presented in Table 10.

Table 10 – Cohesive parameters obtained for the reinforced specimens.

	SPECIMEN	σ_U [MPa]	$\delta_{2,I}$ [mm]	$\sigma_{2,I}$ [mm]	G_{Ic} [N/mm]	E_1 [MPa]	a_0 [mm]
1st TEST	PA12 SCF-1	1.55	0.215	0.635	0.635	2657	46
	PA12 SCF-2	2.35	0.2	0.7	0.65	2907	47.13
	Average	1.95	0.21	0.67	0.64	2782	45.66
3rd TEST	PA12 SCF-1	3.25	0.125	1.5	1.7	2796	37.55
	PA12 SCF-2	1	0.1	0.765	1.435	3038	37.67
	PA12 SCF-3	3.4	0.07	1.85	2.21	3087	37.21
	Average	2.55	0.98	1.44	1.78	2974	37.44
CoV [%]		45.23	44.44	50.47	51.53	6.07	-

As stated in section 5.2, a significant increase in the fracture toughness can be noticed when comparing the results obtained for the first and third batch tests (178%). The same conclusion can be drawn for this material, regarding the conditioning measures implemented for the third batch. However, in this case, a much higher difference can be observed when comparing the two test series, as it is expressed by the CoV value (52%). Since the main difference between the materials is the fibre reinforcement, it can be perceived that its presence influenced the behaviour of the specimen in two different ways. For the first test campaign, a higher local cohesive strength (324%) and lower fracture toughness value (-16.9%) is observed, thus, it can be understood that the reinforced specimen behaviour was more brittle, in comparison to the unreinforced counterparts. The reason for this behaviour may be, in fact, the fibre presence, since, as reported in [20], when the matrix adhesion to the fibre is low, the fibre acts as a brittle inclusion, furtherly reducing the matrix mechanical properties. For this test series, it is to be remembered that no conditioning measures were taken, thus, the influence of the moisture present in the environment may have damaged the interfacial adhesion, which is a behaviour also reported in [26]. Regarding the third test campaign, an increase in the local cohesive strength (264%) and fracture toughness (122.5%) for the reinforced material can be observed, which further sustains the proposed assumption, since this batch of specimens had its conditioning taken into account.

The differences observed did not allow an overall estimate for the fracture toughness of this material. However, for the third test series, all the specimens showed a clear tendency, which was the increasing of the mechanical properties. As stated in section 5.2, the PA12+sCF specimen 3 showed signs of a consecutively pull-out behaviour, which may have increased its fracture toughness even further. Excluding this specimen, the other two show similar results,

which indicates that the fracture toughness of this type of material may be around their average value.

5.4 SEM analysis

For a better understanding of the behaviour differences observed for each type of material and test, a SEM analysis was conducted. Initially, the specimens created for the first series of test were investigated. Figure 55 shows the resulting surfaces of each type of material.

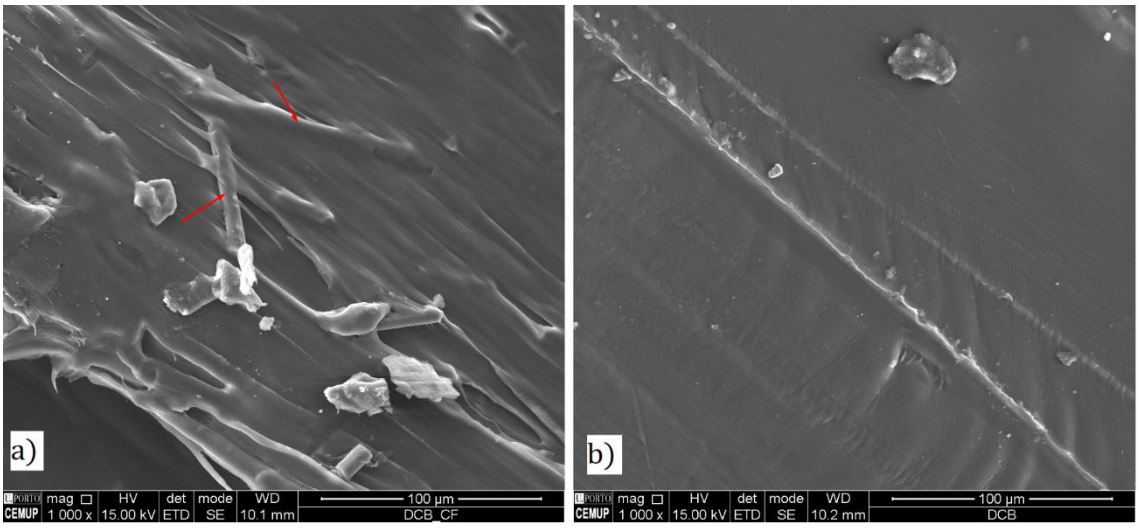

Figure 55 – SEM analysis for the first test series. a) Reinforced specimen. b) Unreinforced specimen.

Overall, it is possible to observe that the reinforced specimen exhibits an irregular surface, while on the other hand, the unreinforced displays a much smoother one. For the reinforced specimen, a high concentration of fibres can be observed on its correspondent surface (evidenced by the red arrows). This type of behaviour was already mentioned in section 2.2.1. It was concluded that this aspect can negatively influence the components interlayer bonding strength, since it indicates that the fibres are not evenly distributed on the deposed filament. In addition, another issue can be appreciated when comparing the resulting surfaces. The reinforced specimen, in comparison with its counterpart, exhibits much more porosity, overall. This effect is also referred in [8], and it is considered to be due to the filament extrusion during the FDM process. Since the carbon fibres are extruded in various positions, the resulting deposed filament is more inconsistent. The association between the two aspects presented (the uneven distribution and the porosity presence) can also be considered as an explanation for the lower values obtained for the reinforced specimens, as the presence of fibres are the cause for the defects shown. Since the third series reinforced specimens exhibited higher values of fracture toughness overall, a comparison between the resulting surfaces of each series specimens was also conducted.

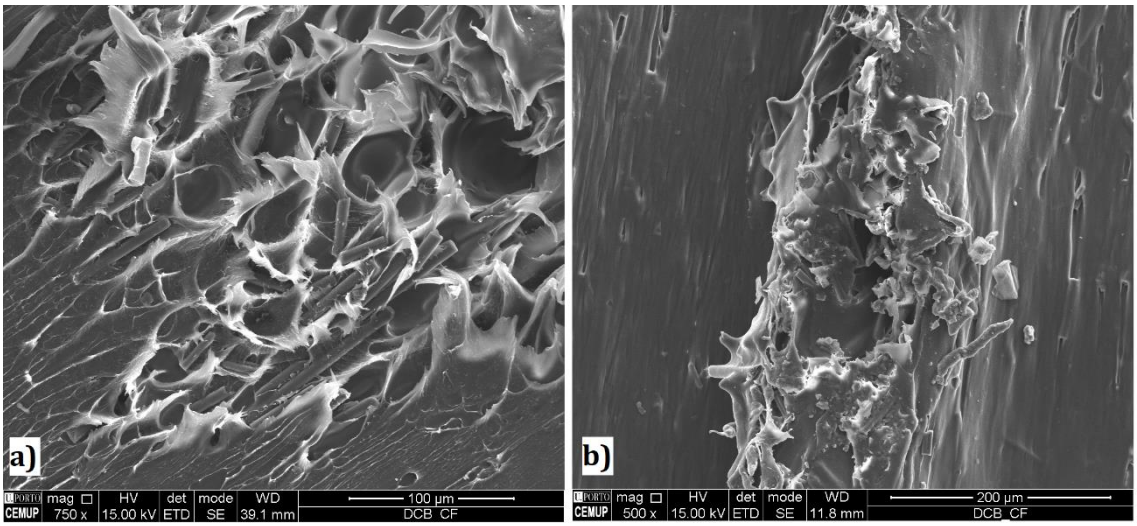

Figure 56 – Comparison of the fractured surfaces, for the reinforced specimens of each series. a) Third series. b) First series.

Figure 56 shows a fractured surface between two adjacent layers, for a reinforced specimen of each series. From this comparison, it can be perceived that the third series show a much higher presence of fibres overall, which indicates that for this series, the fibres were effectively loaded during the test. This comparison can also be used to corroborate the proposed explanation for the increase in the fracture toughness in section 5.2, which distinguished two different types of behaviour for the fibre presence.

5.5 Average cohesive law

In order to verify the accuracy of the obtained results, a numerical simulation was performed applying the average values found for each test and material, which are summarized in Table 11.

Table 11 – Average cohesive parameters and dimensions obtained for each material and test series.

TEST	MATERIAL	L [mm]	B [mm]	H [mm]	a_0 [mm]	σ_U [MPa]	$\delta_{2,I}$ [mm]	$\sigma_{2,I}$ [MPa]	G_{Ic} [N/mm]	E_1 [MPa]
1st	**PA12**	123.9	25.1	5.5	46.9	0.5	1.4	-	0.77	1322
1st	**PA12+sCF**	125.5	25.7	5.6	46.6	2.0	0.2	0.67	0.64	2782
3rd	**PA12**	114.3	25.5	5.4	37.4	0.7	1.0	-	0.80	1953
3rd	**PA12+sCF**	115.0	25.7	5.6	37.5	2.6	0.1	1.37	1.78	2974

The resulting numerical curve obtained for each test was then compared to its experimental counterparts, being the results displayed from Figure 57 to Figure 60.

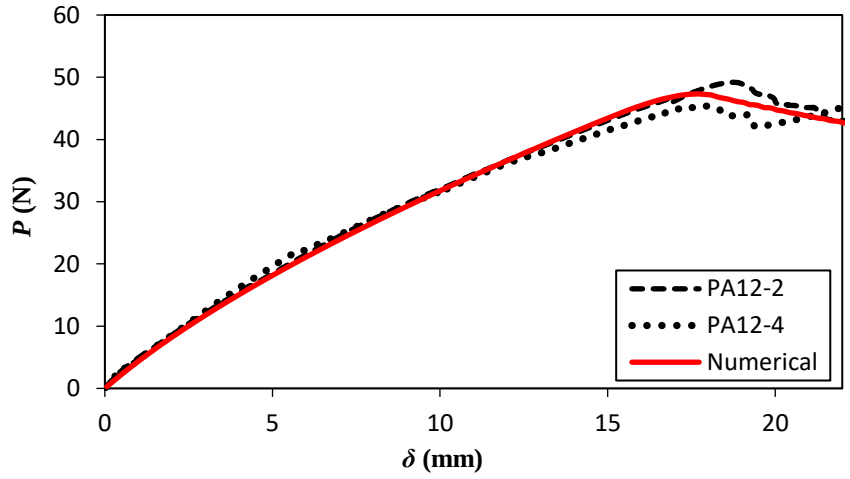

Figure 57 – Comparison of the experimental first series *P*-δ curves and the numerically obtained with its correspondent average cohesive law, for PA12.

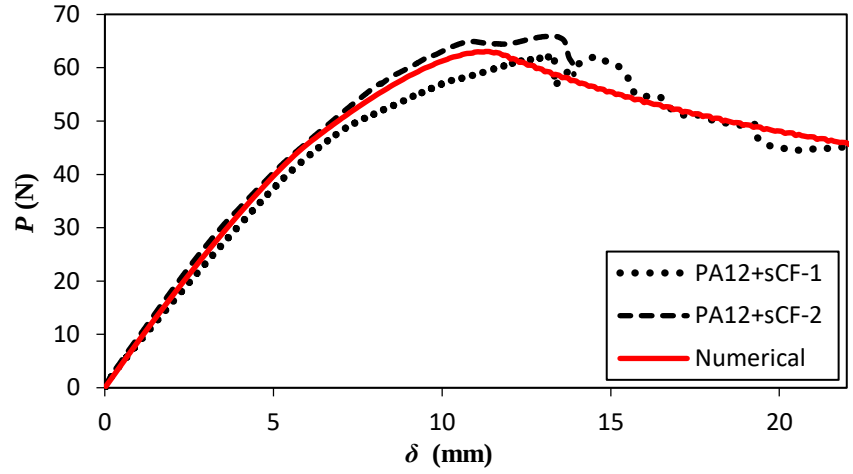

Figure 58 – Comparison of the experimental first series *P*-δ curves and the numerically obtained with its correspondent average cohesive law, for PA12+sCF.

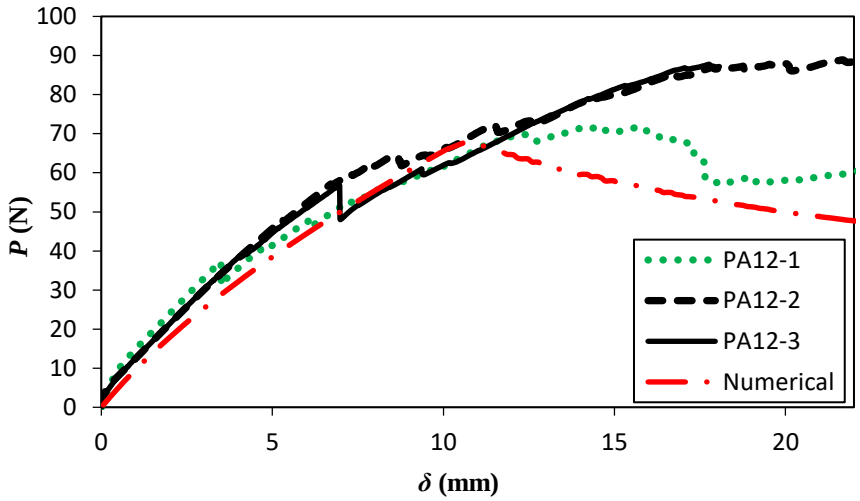

Figure 59 – Comparison of the experimental third series *P*-δ curves and the numerically obtained with its correspondent average cohesive law, for PA12.

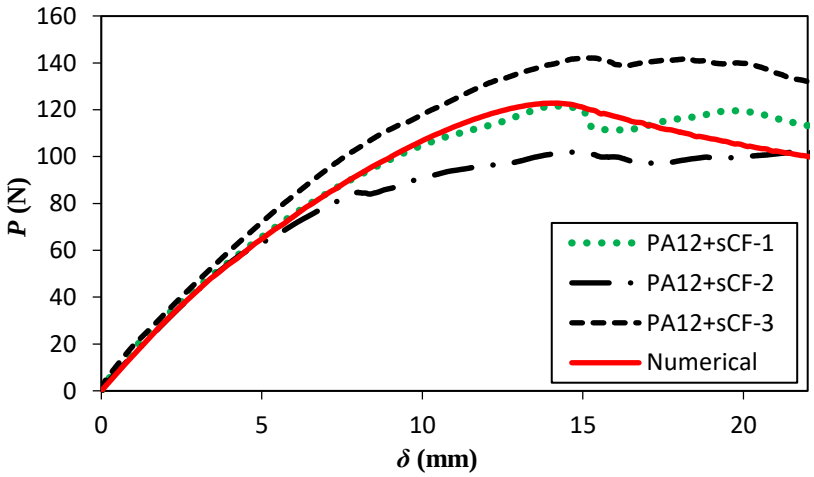

Figure 60 – Comparison of the experimental third series *P*-δ curves and the numerically obtained with its correspondent average cohesive law, for PA12+sCF.

As seen in the figures presented, the numerical simulation provided by the average values displays accurate results, since the behaviour observed in all the cases tested is similar to the one shown by the experimental results. From this fact, it can be concluded that the cohesive laws applied for the simulations are adequate to describe the crack development in mode I, for these materials. Analysing each figure separately, it can also be observed that the only test for which the simulation did not provide an accurate result (meaning that the values obtained for it are not in the mean of the experimental results) was the third test series for the PA12 specimens. The reason for this is the fact that this set of values shows a generalized

unstable behaviour for the duration of the test, which could be explained by flaws in the specimen production process, or by an excessively high opening rate imposed during the DCB test.

5.6 Cohesive diagrams

For a further comparison of the cohesive parameters obtained, a cohesive diagram was plotted, based on the average values found for each material and test, as presented in Table 11. The aim here was to compare both tests for the same material, by superposition of the created diagrams, in order to investigate the veracity of the proposed assumptions for the behaviour differences in each material.

5.6.1 Trapezoidal law – PA12 specimens

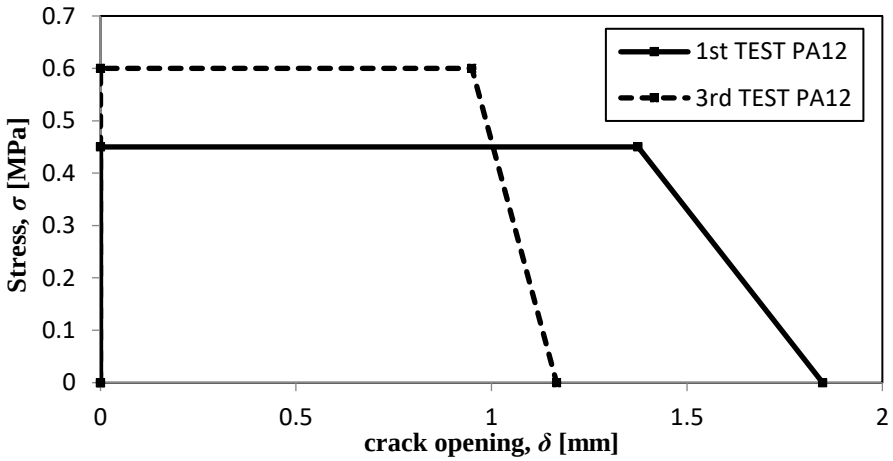

Figure 61 – Plotted trapezoidal diagrams, resulting from the obtained average cohesive law for each series of the PA12 specimens.

As it can be verified from the different shape presented by the diagrams, the cohesive law that describes the behaviour of the specimens is different from the first to the third test, furtherly supporting the theory presented in section 5.3. Since this slight difference was able to be perceived by the differences in shape, it can also be perceived that this type of analysis is able to capture well the behaviour of the material, which sustains the proposition that it is adequate for this type of material.

5.6.2 Bi-linear stress softening law – PA12+sCF specimens

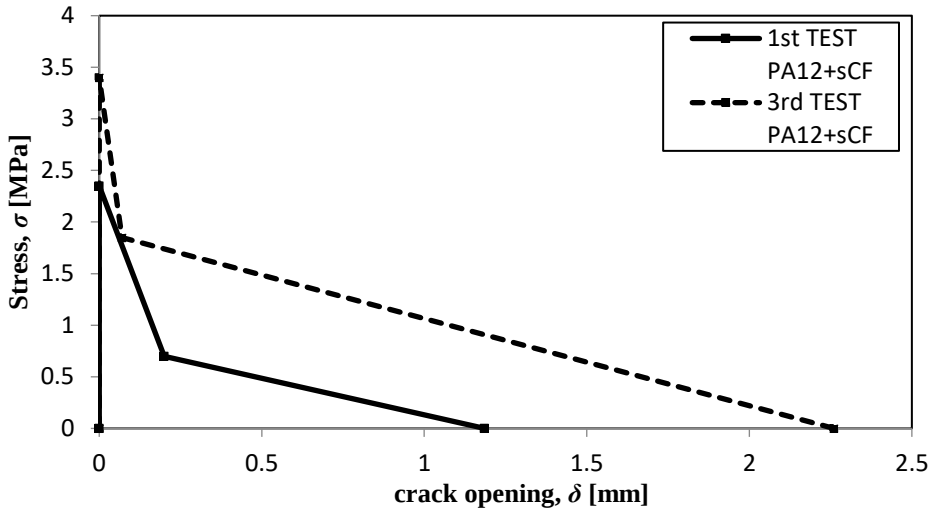

Figure 62 – Plotted bilinear diagrams, resulting from the obtained average cohesive law for each series of the PA12+sCF specimens.

For this case, a greater discrepancy between shapes can be noticed, which goes accordingly with what was observed from the experimental tests. As stated in [37], the bilinear stress softening allows the differentiation between two events, which induce crack propagation. This is accounted by the two different slopes observed, and for the material applied in it (wood), it is due to micro-cracking and fibre bridging phenomena, respectively. In this material and production process, however, the later is not able to occur, and so, its existence is due to another event. When comparing the resulting surfaces after the crack propagation, it was verified that the third series exhibited pulled out layers in a larger quantity than the first test counterparts (see Figure 54), thus, it can be assumed that this type of behaviour is associated with the region defined by the slope after the second inflection point of the law. It was also observed, in section 5.4, that the fibre presence affected the type of interlayer bond in two different ways. By observation of the plotted cohesive diagrams, the same can also be verified, since the mean inflection points position also changed for this series, and in a way that goes accordingly with what was observed in the data obtained. This can also be used to sustain the assumption that this cohesive model is adequate for the characterization of reinforced materials within the FDM technology.

The average parameter values presented in Table 11deserve a special comment. In fact, it is verified that these materials reveal a quite low cohesive strength and Young modulus when compared with traditional composites. However, a special remark should be done about the fracture toughness under mode I loading, whose values are in the range of 0.64-1.8 N/mm. These values are much higher than the ones of typical thermoset composites, usually in the range of 0.3-0.5 N/mm. This reveals that these materials have a potential of application, namely when interlaminar fracture behaviour under mode I loading is a crucial design parameter to take into account.

6 Concluding remarks

6.1 Conclusions

In this dissertation, a method for the characterization of FDM printed components interlaminar fracture under mode I loading was studied. Firstly, a specimen geometry was dimensioned, taking into account the mechanical properties of the materials applied and following the guidelines presented in the ASTM D5528 standard. Double cantilever beam (DCB) tests were performed in the resulting specimens, followed by an analysis of the experimental data obtained from these tests, by application of the compliance-based beam method (CBBM) as a suitable data reduction scheme. Afterwards, scanning electron microscopy (SEM) and optical microscopy were applied in order to analyse the microstructure of the specimens resulting surfaces. For a further characterization of the material's behaviour, a numerical model of the DCB test was developed, in which a process of iteration was employed in order to obtain a set of cohesive parameters, which replicated the experimental data. Two cohesive laws were implemented to this end, regarding the differences between the materials used; the trapezoidal law for the PA12 specimens, and the bilinear stress softening law for PA12+sCF specimens. The results obtained indicated a consistent estimation for the PA12 specimens fracture toughness, while the estimation for the PA12+sCF specimens revealed itself as inconclusive, due to major differences between the data obtained for the two series investigated. Still, the analysis on the behaviour differences for these specimens allowed assuming that the main cause for this was the fibre presence. This conclusion can also present itself as a useful step towards a more efficient production method, since it can be used to acknowledge a series of variables, which are of great influence in the interlayer bonding strength of these type of components. As for the cohesive models applied, they revealed themselves as an adequate method to characterize this specific type of material and process, since the numerical curves obtained were able to capture well the behaviour of the experimental tests.

6.2 Future works

While it is verified that for the current moment this type of technology is not able to create components with the same type of accuracy or mechanical performance as others which

are already well established, such as compression moulding, it is important to refer that it is yet in a relatively initial phase of development. As it was verified through the course of this dissertation, there are a series of variables, which ultimately influence the efficiency of the component final mechanical properties, rendering the part build mechanism in FDM as a complex process. For this reason, it can be understood that there is still much room for improvement. The conclusions obtained suggest that more efficient production techniques have to be developed in order to enhance the interlayer bonding strength of this type of technology. In this regard, research on the influence of the deposition temperature can be made, for instance, by observation of a series of components created with distinct ones. Another set of variables which can be heavily manipulated are the FDM printing parameters, such as raster orientation or layer thickness, and for this reason, the analysis of its influence is also an important step to be made.

References

[1] Z. Quan *et al.*, "Additive manufacturing of multi-directional preforms for composites: Opportunities and challenges," *Mater. Today*, vol. 18, no. 9, pp. 503–512, 2015.

[2] M. Nikzad, S. H. Masood, and I. Sbarski, "Thermo-mechanical properties of a highly filled polymeric composites for Fused Deposition Modeling," *Mater. Des.*, vol. 32, no. 6, pp. 3448–3456, 2011.

[3] F. Ning, W. Cong, J. Qiu, J. Wei, and S. Wang, "Additive manufacturing of carbon fiber reinforced thermoplastic composites using fused deposition modeling," *Compos. Part B Eng.*, vol. 80, pp. 369–378, 2015.

[4] O. A. Mohamed, S. H. Masood, and J. L. Bhowmik, "Analytical modelling and optimization of the temperature-dependent dynamic mechanical properties of fused deposition fabricated parts made of PC-ABS," *Materials (Basel).*, vol. 9, no. 11, 2016.

[5] M. Spoerk, F. Arbeiter, H. Cajner, J. Sapkota, and C. Holzer, "Parametric optimization of intra- and inter-layer strengths in parts produced by extrusion-based additive manufacturing of poly (lactic acid)," vol. 45401, pp. 1–15, 2017.

[6] Y. Zhang and K. Chou, "A parametric study of part distortions in fused deposition modelling using three-dimensional finite element analysis," *Proc. Inst. Mech. Eng. Part B J. Eng. Manuf.*, vol. 222, no. 8, pp. 959–967, 2008.

[7] B. Brenken, E. Barocio, A. Favaloro, V. Kunc, and R. B. Pipes, "Fused filament fabrication of fiber-reinforced polymers: A review," *Addit. Manuf.*, vol. 21, no. October 2017, pp. 1–16, 2018.

[8] C. Bellehumeur and L. Li, "Modeling of Bond Formation Between Polymer Filaments in the Fused Deposition Modeling Process," *J. Manuf. Process.*, vol. 6, no. 2, pp. 170–178, 2004.

[9] A. K. Sood, R. K. Ohdar, and S. S. Mahapatra, "Parametric appraisal of mechanical property of fused deposition modelling processed parts," *Mater. Des.*, vol. 31, no. 1, pp. 287–295, 2010.

[10] W. Zhang *et al.*, "Characterization of residual stress and deformation in additively manufactured ABS polymer and composite specimens," *Compos. Sci. Technol.*, vol. 150, pp. 102–110, 2017.

[11] J. P. Lewicki *et al.*, "3D-Printing of Meso-structurally Ordered Carbon Fiber/Polymer Composites with Unprecedented Orthotropic Physical Properties," *Sci. Rep.*, vol. 7, no. January, pp. 1–14, 2017.

[12] W. Zhang *et al.*, "Interfacial bonding strength of short carbon fiber/acrylonitrile-butadiene-styrene composites fabricated by fused deposition modeling," *Compos. Part*

B Eng., vol. 137, no. October 2017, pp. 51–59, 2018.

[13] M. S. Islam and P. Prabhakar, "Interlaminar strengthening of multidirectional laminates using polymer additive manufacturing," *Mater. Des.*, vol. 133, pp. 332–339, 2017.

[14] Fillamentum, "Technical data sheet: Nylon FX256," 2011. [Online]. Available: https://fillamentum.com/products/nylon-fx256-natural. [Accessed: 27-Mar-2018].

[15] Fillamentum, "Technical data sheet: Nylon CF15 Carbon," 2017. [Online]. Available: https://fillamentum.com/collections/technical-polymers/products/nylon-cf15-carbon. [Accessed: 27-Mar-2018].

[16] C. Ziemian, M. Sharma, and S. Ziemi, "Anisotropic Mechanical Properties of ABS Parts Fabricated by Fused Deposition Modelling," *Mech. Eng.*, 2012.

[17] N. Aliheidari, J. Christ, and A. Ameli, "Measuring the interlayer fracture resistance of FDM printed thermoplastics," *Soc. Plast. Eng. ANTEC*, pp. 5–9, 2016.

[18] J. M. J. M. Pearce *et al.*, "Mechanical properties of components fabricated with open-source 3-D printers under unrealistic environmental conditions," *Mater. Des.*, vol. 58, pp. 242–246, 2014.

[19] T. Hofstätter, D. B. Pedersen, G. Tosello, and H. N. Hansen, "Applications of Fiber-Reinforced Polymers in Additive Manufacturing," *Procedia CIRP*, vol. 66, pp. 312–316, 2017.

[20] D. Young, J. Kessler, and M. Czabaj, "Interlayer Fracture Toughness of Additively Manufactured Unreinforced and Carbon-Fiber-Reinforced Acrylonitrile Butadiene Styrene," *Am. Soc. Compos. Thirty-First Tech. Conf.*, 2016.

[21] J. Duchoslav, C. Unterweger, R. Steinberger, C. Fürst, and D. Stifter, "Investigation on the thermo-oxidative stability of carbon fiber sizings for application in thermoplastic composites," *Polym. Degrad. Stab.*, vol. 125, pp. 33–42, 2016.

[22] A. N. Dickson, J. N. Barry, K. A. McDonnell, and D. P. Dowling, "Fabrication of continuous carbon, glass and Kevlar fibre reinforced polymer composites using additive manufacturing," *Addit. Manuf.*, vol. 16, pp. 146–152, 2017.

[23] E. C. Botelho, Figiel, M. C. Rezende, and B. Lauke, "Mechanical behavior of carbon fiber reinforced polyamide composites," *Compos. Sci. Technol.*, vol. 63, no. 13, pp. 1843–1855, 2003.

[24] S. S. Yao, F. L. Jin, K. Y. Rhee, D. Hui, and S. J. Park, "Recent advances in carbon-fiber-reinforced thermoplastic composites: A review," *Compos. Part B Eng.*, vol. 142, no. July 2017, pp. 241–250, 2018.

[25] D. P. N. Vlasveld, J. Groenewold, H. E. N. Bersee, and S. J. Picken, "Moisture absorption in polyamide-6 silicate nanocomposites and its influence on the mechanical properties," *Polymer (Guildf).*, vol. 46, no. 26, pp. 12567–12576, 2005.

[26] V. T. Do, H. D. Nguyen-Tran, and D. M. Chun, "Effect of polypropylene on the mechanical properties and water absorption of carbon-fiber-reinforced-polyamide-6/polypropylene composite," *Compos. Struct.*, vol. 150, pp. 240–245, 2015.

[27] N. Aliheidari, R. Tripuraneni, A. Ameli, and S. Nadimpalli, "Fracture resistance measurement of fused deposition modeling 3D printed polymers," *Polym. Test.*, vol. 60, pp. 94–101, 2017.

[28] L. Nicolais, M. F. S. F. de Moura, and R. M. Guedes, "Fracture: Interlaminar," *Wiley*

Encyclopedia of Composites. John Wiley & Sons, Inc., pp. 1–11, 2011.

[29] A. A. Griffith, "The phenomenon of rupture and flow in solids," *Philos Trans R Soc L.*, vol. 221, pp. 163–198, 1920.

[30] ASTM D-5528-94a, "Standard Test Method for Mode I Interlaminar Fracture Toughness of Unidirectional Fiber-Reinforced Polymer Matrix Composites," *Annu. B. ASTM Stand.*, vol. 01, no. Reapproved 2007, pp. 271–279, 1994.

[31] S. in Park, N. Watanabe, and D. W. Rosen, "Estimating failure of material extrusion truss structures based on deposition modeling and a cohesive zone model," *Mater. Des.*, vol. 147, pp. 122–133, 2018.

[32] G. F. Dias, M. F. S. F. de Moura, J. A. G. Chousal, and J. Xavier, "Cohesive laws of composite bonded joints under mode I loading," *Compos. Struct.*, vol. 106, pp. 646–652, 2013.

[33] M. F. S. F. de Moura, J. J. L. Morais, and N. Dourado, "A new data reduction scheme for mode I wood fracture characterization using the double cantilever beam test," *Eng. Fract. Mech.*, vol. 75, no. 13, pp. 3852–3865, 2008.

[34] C. Dudescu and L. Racz, "Effects of Raster Orientation, Infill Rate and Infill Pattern on the Mechanical Properties of 3D Printed Materials," *ACTA Univ. Cibiniensis*, vol. 69, no. 1, 2017.

[35] R. Taktak, N. Guermazi, J. Derbeli, and N. Haddar, "Effect of hygrothermal aging on the mechanical properties and ductile fracture of polyamide 6: Experimental and numerical approaches," *Eng. Fract. Mech.*, vol. 148, pp. 122–133, 2015.

[36] M. F. S. F. De Moura and J. A. G. Chousal, "Simulation of Bonded Joints Failure using Progressive Mixed-Mode," pp. 147–170.

[37] N. Dourado, S. Morel, M. F. S. F. de Moura, G. Valentin, and J. Morais, "Comparison of fracture properties of two wood species through cohesive crack simulations," *Compos. Part A Appl. Sci. Manuf.*, vol. 39, no. 2, pp. 415–427, 2008.

APPENDIX A: Gantt chart

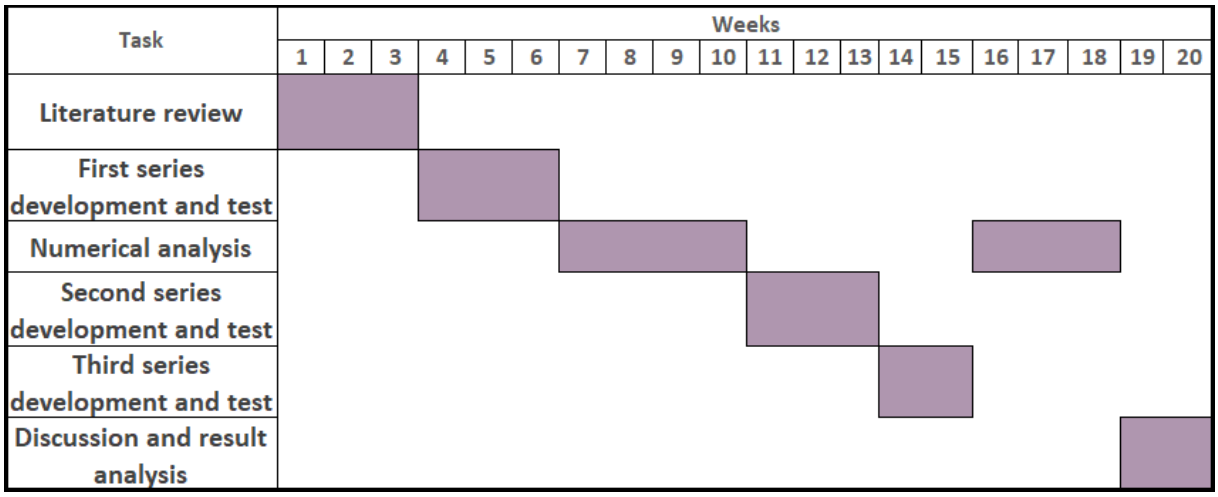

Figure 63 – Gantt chart of the steps taken in the dissertation.